# Sea surface topography fields of the tropical Pacific from data assimilation

Robert N. Miller

College of Oceanic and Atmospheric Sciences, Oregon State University, Corvallis

Antonio J. Busalacchi

Laboratory for Hydrospheric Processes, NASA Goddard Space Flight Center, Greenbelt, Maryland

Eric C. Hackert

Hughes STX Corporation and Laboratory for Hydrospheric Processes, NASA Goddard Space Flight Center, Greenbelt, Maryland

**Abstract.** Time series of maps of monthly tropical Pacific dynamic topography anomalies from 1979 through 1985 were constructed by means of assimilation of tide gauge and expendable bathythermograph (XBT) data into a linear model driven by observed winds. Estimates of error statistics were calculated and compared to actual differences between hindcasts and observations. Four experiments were performed as follows: one with no assimilation, one with assimiation of sea level anomaly data from eight selected island tide gauge stations, one with assimilation of dynamic height anomalies derived from XBT data, and one with both XBT and tide gauge data assimilated. Data from seven additional tide gauge stations were withheld from the assimilation process and used for verification in all four experiments. Statistical objective maps based on data alone were also constructed for comparison purposes. The dynamic response of the model without assimilation was, in general, weaker than the observed response. Assimilation resulted in enhanced signal amplitude in all three assimilation experiments. RMS amplitudes of statistical objective maps were only strong near observing points. In large data-void regions these maps show amplitudes even weaker than the wind-driven model without assimilation. With few exceptions the error estimates generated by the Kalman filter appeared quite reasonable. Since the error processes cannot be assumed to be white or stationary, we could find no straightforward way to test the formal statistical hypothesis that the time series of differences between the filter output and the actual observations were drawn from a population with statistics given by the Kalman filter estimates. The autocovariance of the innovation sequence, i.e., the sequence of differences between forecasts before assimilation and observations, has long been used as an indicator of how close a filter is to optimality. We found that the best filter we could devise was still short of the goal of producing a white innovation sequence. In this and earlier studies, little sensitivity has been found to the parameters under our direct control. Extensive changes in the assumed error statistics make only marginal differences. The same is true for long time and space scale behavior of different models with richer physics and finer resolution. Better data assimilation results will probably require relaxation of the assumptions of stationarity and serial independence of the errors. Formulation of such detailed noise models will require longer time series, with the attendant problems of matching very different data sets.

## 1. Introduction

In an earlier study, *Miller and Cane* [1989] (hereinafter referred to as MC) produced maps of sea level height in the Pacific from 1979 to 1983 based on tide

gauge data and a simple dynamical model driven by analyzed monthly mean wind fields derived from merchant ship observations [*Stricherz et al.*, 1992]. In that study, coastal and near-equatorial tide gauge data were assimilated by the Kalman filter [e.g., *Miller*, 1986; *Ghil et al.*, 1981]. The maps revealed richer structure than could have been inferred from the model output or the data alone. The error estimates derived from that study can be considered reliable (see, especially, *Miller* [1990]),

which leads us to conclude that the structure observed in the Kalman filter analysis is probably present in nature.

MC was based on assimilation of data at only six tide gauge stations, with records from four additional tide gauge stations held back from the assimilation process for verification. The simple wave model used in that study was designed with economical implementation of the Kalman filter as a goal. With only 384 state variables it was practical to perform a large number of experiments (recall that the high computational overhead associated with the Kalman filter stems from calculation of the covariance evolution, which involves an amount of work proportional to the square of the dimension of the state vector). This model was limited in scope, based as it was on a slowly converging expansion in Hermite functions in the meridional direction. Five Rossby modes were used in that model, which implies, in turn, that the meridional structure was defined in terms of the Hermite functions of degrees up to 6. Relative to the equatorial deformation radius for the first baroclinic mode, the most poleward root of the Hermite function of degree 6 is approximately 6°, which means that the model is only to be trusted in a narrow band of latitudes near the equator.

In the present study we use the Kalman filter implemented with the grid point model of *Cane and Patton* [1984] (hereinafter referred to as CP). In the CP model the Hermite expansion is replaced by a finite difference approximation throughout the domain, which is a more accurate representation of the dynamics poleward of about 4°, even for very coarse grids. Effects of the artificial solid boundaries at 29°N and 29°S limit the reliability of this model poleward of about 15°, but comparisons to dynamic height observations show some skill as far poleward as 20°. Tests of the model over a wide range of computational parameters show these effects, which consist mainly of trapped waves near the artificial boundaries, to be highly dependent on resolution. This enlarged region of validity of the CP model over the MC model allows us to assimilate the entire set of dynamic height data derived from the Tropical Oceans and Global Atmosphere (TOGA) expendable bathythermograph (XBT) sections [*Picaut et al.*, 1991], in addition to the tide gauge data.

It is one of our major purposes to explore the practical details of assimilation of different types of data to guide us toward use of data from arrays of moored instruments such as the Tropical Atmosphere Ocean (TAO) array [see *Hayes et al.*, 1991] and satellite altimetric data. This is a necessary step on the way to providing analyses of all fields of interest based on all available data.

Another major goal of this study is to explore the limits of the simple models of error statistics used in previous studies. Most data assimilation studies we know of include, implicitly or explicitly, the assumption of stationary homogeneous white additive noise (but see *Budgell* [1987] and *Daley* [1992a]). It is, in practice, further assumed that the noise is independent of the model state itself. We know all of these hypotheses to be false to some degree. It should be noted here that statistical error models are contained explicitly in the formulation of adjoint and optimal interpolation methods, as well as the Kalman filter. Here we discard the assumption of homogeneity of the wind error covariance field and construct a statistical error model which is inhomogeneous in space.

Section 2 contains a brief description of the model and the data assimilation scheme; section 3 contains a description of the data sets used. Details of the error model are discussed in section 4. Results are presented in section 5, and section 6 contains discussion and summary.

## 2. The Model and the Data Assimilation Scheme

### 2.1. The Model

The model described in CP is a finite difference model of the linear shallow water equations on an equatorial beta plane. The equations for each baroclinic mode, further simplified by a long wave approximation, are given by

$$\begin{aligned}
u_t - yv + h_x &= F \\
yu + h_y &= G \\
h_t + u_x + v_y &= Q
\end{aligned}$$

where $x$ and $y$ are distances in the zonal and meridional directions, $u$ and $v$ are the zonal and meridional velocity components, $h$ is the sea level height increment, and $t$ is time. Lengths have been scaled by the equatorial deformation radius $(c/\beta)^{1/2}$, and times by $(c\beta)^{-1/2}$, where $c$ is the Kelvin wave speed for the vertical mode in question and $\beta$ is the rate of change of the Coriolis acceleration with latitude. The Kelvin wave speed $c$ is assumed constant in time and space. The external forcings $F$, $G$, and $Q$ include zonal wind stress, meridional wind stress, and buoyancy flux, respectively. They also include parameterized diffusion of momentum and buoyancy. In this study, buoyancy flux and meridional wind stress are neglected. This assumption is supported by dimensional arguments and by earlier studies [e.g., MC, *Miller*, 1990] which showed that errors in the zonal wind stress could account for all of the errors in previous models. This assumption results in considerable simplification of the error model. The most obvious cost is the loss of accuracy along the eastern and western boundaries. In the absence of meridional winds the height anomaly along the eastern boundary is constant. This follows from the meridional momentum equation. In reality, there are local variations along the coast of south and central America due to a balance between local meridional winds and the slope of the sea level height. This is not significant at Callao, but it is quite significant at several other sea level stations.

In order to keep the dimension of the state space as small as possible, a very coarse grid is used. The model

used here has zonal resolution of 5° and meridional resolution of 2°. The time step was 10 days. We compared this coarse resolution model to a test run with grid spacing halved in both directions. The RMS difference in the height anomaly fields between the coarse and fine resolution runs was less than 2 cm from 10°S to 10°N over most of the basin, reaching 3 cm only in small regions north of 15°N and west of 170°E and south of 17°S and west of 160°W. Further comparisons with a nonlinear primitive equation model with grid spacing of 1/3° × 1/3° showed similarly small differences with similar spatial distribution. Two vertical modes are considered, with speeds derived from *Eriksen et al.* [1983]. The Kelvin wave speeds for the first and second modes were 2.91 and 1.78 m/s, respectively. The resulting time and space scales are 1.42 days and 3.22° for the first mode and 1.82 days and 2.52° for the second. Linear damping was added in the form of Rayleigh friction, with decay times of 30.0 months and 11.0 months for the first and second baroclinic modes, respectively. A series of comparison runs showed little sensitivity to decay times greater then 6.0 months. The model domain was a rectangular box, extending from 125°E to 80°W and from 29°S to 29°N. Further details of the model are given by CP.

Dissipation is added in the form of a Shapiro filter [*Shapiro,* 1971] in order to suppress grid scale noise which is continually excited during the assimilation process. The assimilation process introduces data on scales which are comparable to the grid spacing in this coarse model, and the small scale waves which are excited would persist if they were not explicitly suppressed. This effect is especially pronounced near boundaries, where waves are excited which propagate as trapped waves near the artificial northern and southern boundaries. This could be ameliorated considerably by using open boundary conditions [e.g., *Busalacchi and Blanc,* 1989], but the mass fluxes so generated would affect the total mass balances over several years of model time. It would then become necessary to formulate some realistic method for keeping track of the mass balance. This would add considerably to the complexity of the model and add little to the usefulness of the results. The Shapiro filter is applied to the entire state vector, thus functioning as a high-order diffusivity of mass and momentum. The effect of the Shapiro filter on model sea level is negligible. The large-scale structure of the model fields within 15° of the equator is not sensitive to the filter.

## 2.2. The Data Assimilation Scheme

The data assimilation method used here is the Kalman filter, which has been described in detail in many places [e.g., *Gelb,* 1974]. The Kalman filter was first formulated in the meteorological context by *Ghil et al.* [1981] and later applied to ocean modeling by a number of investigators [e.g., *Bennett and Budgell,* 1989; *Miller,* 1986; *Gaspar and Wunsch,* 1989; *Miller and Cane,* 1989; *Miller,* 1990]. The Kalman filter is a filter in the sense used conventionally in the time series

literature, i.e., a method for finding the optimal estimate of the state of a system at a designated time (the "present"), given a set of prior (i.e., "past") observations. Methods which make use of all data, including observations at times beyond the designated time (the "future") are known as "smoothers." Practical smoothers are constructed by minimizing some positive definite functional (the "cost function") of the history of the state vector [e.g., *Bennett and Budgell,* 1989; *Bennett,* 1990, 1992]. The minimization process is conveniently formulated in terms of the adjoint of the evolution operator. For this reason, these methods are often referred to as "adjoint methods" in the literature [e.g., *Ghil and Malanotte-Rizzoli,* 1991]. A derivation of the precise relation between the Kalman filter and variational smoothing methods is given by *Bennett and Budgell* [1989], who applied it to a linearized quasi-geostrophic model. *Fu et al.* [1993] used a variational smoother to assimilate Geosat altimeter data into the simple model presented in MC and found that the results differed little from those obtained from the Kalman filter. Since the Kalman filter and Kalman smoother gave similar results in that study, we chose to use the Kalman filter here because of its lower computational complexity and resource demands.

The Kalman filter, as implemented here, is described as follows: let $\mathbf{w}$ be the state vector, which completely specifies the model. The numerical model can be written as

$$\mathbf{w}^f_{k+1} = \mathbf{L}\mathbf{w}^a_k + \tau_k \qquad (1)$$

where subscripts denote time step, superscript $f$ denotes "forecast," and superscript $a$ denotes "analysis," the best available estimate of the state vector at time $t_k$. The vector $\tau_k$ is the forcing at time $t_k$. The transition matrix $\mathbf{L}$ represents the numerical scheme for the state evolution.

The model is assumed to differ from the true system by random noise, i.e., the underlying dynamics obey

$$\mathbf{w}^t_{k+1} = \mathbf{L}\mathbf{w}^t_k + \tau_k + \mathbf{b}_k$$

where the quantities with the superscript $t$ represent the true system. Here $\mathbf{b}_k$ is a white sequence with covariance given by

$$\langle \mathbf{b}_j \mathbf{b}_k^T \rangle = \mathbf{Q}\delta_{jk}$$

where angle brackets denote expected value and $\mathbf{Q}$ is a positive definite matrix known as the "system noise covariance." The superscript $T$ denotes transpose.

The observations $\mathbf{w}^o_{k+1}$ are related to the true state vector $\mathbf{w}^t_{k+1}$ by

$$\mathbf{w}^o_{k+1} = \mathbf{H}_{k+1}\mathbf{w}^t_{k+1} + \mathbf{b}^o_{k+1}$$

where $\mathbf{b}^o_{k+1}$ is the observation error, which is assumed to be a white sequence with zero mean and covariance given by $\langle \mathbf{b}^o_{k+1}\mathbf{b}^{oT}_{k+1} \rangle = \mathbf{R}_{k+1}$. $\mathbf{H}_k$, the observation matrix, is linear transformation which relates the state variables to the observed quantities. The forecast error

covariance $\mathbf{P}_k^f$ is defined by

$$\mathbf{P}_k^f = \left\langle \left(\mathbf{w}_k^t - \mathbf{w}_k^f\right)\left(\mathbf{w}_k^t - \mathbf{w}_k^f\right)^T \right\rangle$$

The analysis error $\mathbf{P}_k^a$ is defined similarly. The evolution of the forecast error covariance is given by

$$\mathbf{P}_{k+1}^f = \mathbf{L}\mathbf{P}_k^a\mathbf{L}^T + \mathbf{Q} \tag{2}$$

The updated state vector is given by

$$\mathbf{w}_{k+1}^a = \mathbf{w}_{k+1}^f + \mathbf{K}_{k+1}(\mathbf{w}_{k+1}^o - \mathbf{H}_{k+1}\mathbf{w}_{k+1}^f) \tag{3}$$

where $\mathbf{K}_{k+1}$ is the Kalman gain matrix

$$\mathbf{K}_{k+1} = \mathbf{P}_{k+1}^f\mathbf{H}_{k+1}^T\left(\mathbf{H}_{k+1}\mathbf{P}_{k+1}^f\mathbf{H}_{k+1}^T + \mathbf{R}_{k+1}\right)^{-1} \tag{4}$$

The error covariance of the updated field is given by

$$\mathbf{P}_{k+1}^a = (\mathbf{I} - \mathbf{K}_{k+1}\mathbf{H}_{k+1})\mathbf{P}_{k+1}^f \tag{5}$$

Equations (1)–(5) define explicitly the process by which the evolution of the model state $\mathbf{w}$ and its error covariance $\mathbf{P}$ are calculated, with updating when observations are available. Note that in the absence of updating, the system noise covariance matrix $\mathbf{Q}$ is the only forcing term in the evolution of $\mathbf{P}$ and that the dependence of $\mathbf{P}$ on $\mathbf{Q}$ in that case is linear.

Reliable error estimates are a major objective of the present study, as they were in the work of *Gaspar and Wunsch* [1989]. It is important to note that similar error estimates would result from other data assimilation methods if the same statistical noise model were used.

## 3. The Data

### 3.1. Wind Data

The wind data used here come from a monthly pseudostress analysis from merchant ship observations [*Stricherz et al.*, 1992] provided by Florida State University. Hereafter, this data set will be referred to as FSU. The FSU data set was further processed as follows [see *Zebiak*, 1989]: a 4-year running monthly mean was removed from the raw wind analysis; so, for example, in order to produce the pseudostress anomaly data for a given January, the average of the data from the current January plus the January data from the three previous years is subtracted. This is done to remove a long-term trend which is known to appear in the data over a time span longer than the period of interest [cf. *Zebiak*, 1989]. The resulting anomaly data set was then filtered with a 1-2-1 filter in latitude, longitude, and time.

Little is known about the error characteristics of the FSU analysis. *Chelton and O'Brien* [1982] compared Seasat scatterometer winds with this analysis. Their work suggests highly spatially inhomogeneous wind stress analysis error with magnitude (about 2 m/s RMS), consistent with *Halpern and Harrison's* [1982]

study comparing a number of different wind products for a single month and with the later study of *Reynolds et al.* [1989]. Data coverage for the FSU wind analysis is concentrated along major shipping routes; examples of an observing pattern for the FSU analysis are given by *Reynolds et al.* [1989] and *Legler and O'Brien* [1985]. One naturally expects the analysis to be most accurate in these regions.

Difference fields between the FSU analysis and analyses derived from remote sensing corroborate this view outside of a few small regions. *Busalacchi et al.* [1989] show a comparison of the FSU data set with SAWIN, an analysis based on cloud motion vectors east of the date line and surface data elsewhere [*Sadler and Kilonsky*, 1985; *Sadler et al.*, 1987]. One expects the differences between these two wind data sets to be small west of the date line, where they are based on similar data. However, a similar pattern appears in comparisons of the FSU data set with SAWIN east of the date line. This pattern also agrees with comparison to a wind data set based on the special sensor microwave/imager (SSM/I) data, courteously provided by R. Atlas. In regions of sparse surface data coverage, the RMS differences can be as high as 0.35 dyn/cm$^2$, comparable to the signal amplitude. The construction of a statistical model of the wind errors is described in section 4.

### 3.2. Sea Level Data

Data were taken from tide gauges at various locations in the Pacific [*Wyrtki et al.*, 1988]. Unlike previous work [MC; *Miller*, 1990], tide gauge data are not restricted to a narrow band of latitudes, but in this case, with this more flexible model, data from a number of off-equatorial stations are chosen. The locations of the islands are shown in Figure 1. The raw data consist of monthly means with tides removed. The average for each month is removed to yield the monthly mean anomalies.

The tide gauge data can be considered accurate within 3 cm (K. Wyrtki, personal communication, 1986). A number of factors contribute to this error, including local hydraulics and effects of waves from local winds. These effects dominate the inaccuracy in the instrument itself.

### 3.3. Hydrography

The hydrographic data consist of surface dynamic height relative to 400 dbar, processed from XBT casts, through the use of the mean T-S relation from *Levitus* [1982]. These data were gathered into the three tracks shown in Figure 1. Each track represents a general region in which data were grouped into 1-month by 1° latitude bins from 20°S to 20°N with varying zonal width of as much as 24°. The tracks themselves represent the major shipping routes in the region, along which data are concentrated. Details of the processing and aggregation of data are given by *Picaut et al.* [1991] and *Picaut and Tournier* [1991]. As with the sea level data, the average for each month was removed to yield the monthly anomaly data.
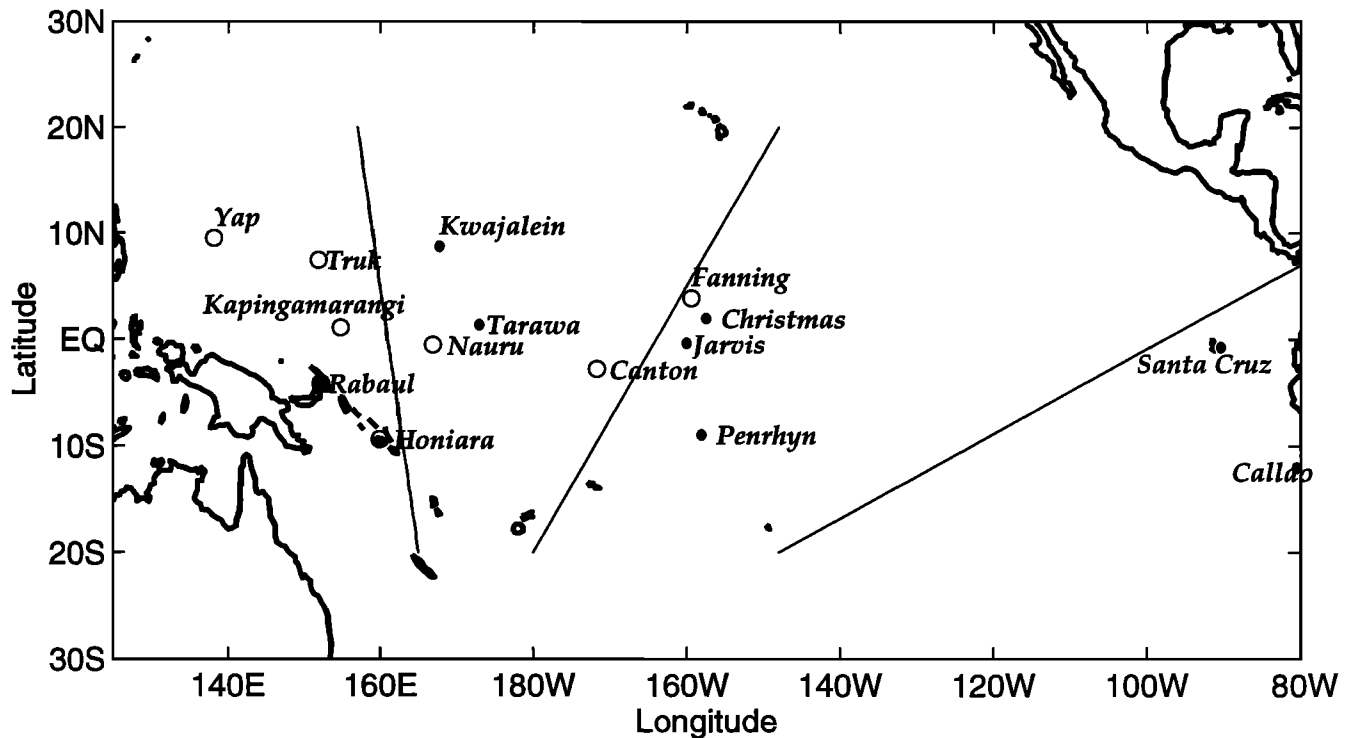
**Figure 1.** The model domain, showing locations of tide gauges and approximate mean positions of expendable bathythermograph (XBT) distributions in the eastern, central, and western Pacific. Solid circles represent assimilation stations, and open circles depict stations held back from the assimilation process for validation.

Errors were assumed to arise from aliasing of internal waves [*Chereskin et al.*, 1986], the use of the mean T-S relation, and the aggregation of casts from wide ranges of longitudes in each bin [*McPhaden et al.*, 1988]. Errors from each source were assumed to have variance of 4 cm$^2$. Errors from different sources were further assumed to be independent. Errors in individual casts from aliasing of internal waves and from the use of the mean T-S relation were also assumed to be independent, and thus the variances of the contributed errors were reduced by factors of the mean number of casts per bin, three in the western section, four in the central section, and two in the eastern section. The error variances in each 1° longitude bin were thus assumed to be 6.7, 6.0, and 8.0 cm$^2$ in the western, central, and eastern sections, respectively.

*Rebert et al.* [1985] compared sea level data with 400-m dynamic height data derived from XBT casts, processed in similar fashion to the data used here. They concluded that sea level data on these timescales essentially reflected 400-m dynamic height increments. The tide gauges in our data set which are closest to the XBT tracks are Fanning and Honiara. Figure 2 shows comparisons of sea level data at these two islands, with dynamic height data from the nearest points on the central and eastern tracks, respectively. The correlations between sea level anomaly and 400-m dynamic height at the nearest data point are 0.90 and 0.80 at Fanning and Honiara, respectively; both these figures are significant at the 99% level. *Rebert et al.* [1985] found

a correlation of 0.80 at Honiara; they did not examine data at Fanning. The RMS differences between the 400-m dynamic height observations and the sea level observations are 4.4 cm and 6.5 cm at Fanning and Honiara, respectively. These numbers are greater than the estimated RMS instrument errors, so measurements at tide gauge stations and dynamic height measurements probably carry some independent information.

Direct assimilation of the raw data, while practical, would be cumbersome due to the sheer number of observations, namely, 41 per track for the western and central tracks and 28 for the eastern track each month. While our experiments show that the condition number of $\left(\mathbf{H}_{k+1}\mathbf{P}^f_{k+1}\mathbf{H}^T_{k+1} + \mathbf{R}_{k+1}\right)^{-1}$, the denominator of the Kalman gain matrix, is only a few hundred, there are, in fact, only a few independent degrees of freedom in each track. This results from the strong meridional correlation of the errors in the model forecasts, which, in turn, reflects the large-scale structure of the error covariance field. We therefore calculated the empirical orthogonal functions (EOFs) of the deviations of the dynamic heights from the monthly mean dynamic heights along each track (see Figure 3). Our EOFs in the central section differ from those shown by *Kessler and Taft* [1987], which are calculated from the deviations from the along-track climatological means and contain the seasonal cycle.

In our experiments we retain the four leading EOFs in each track. The RMS differences between the raw
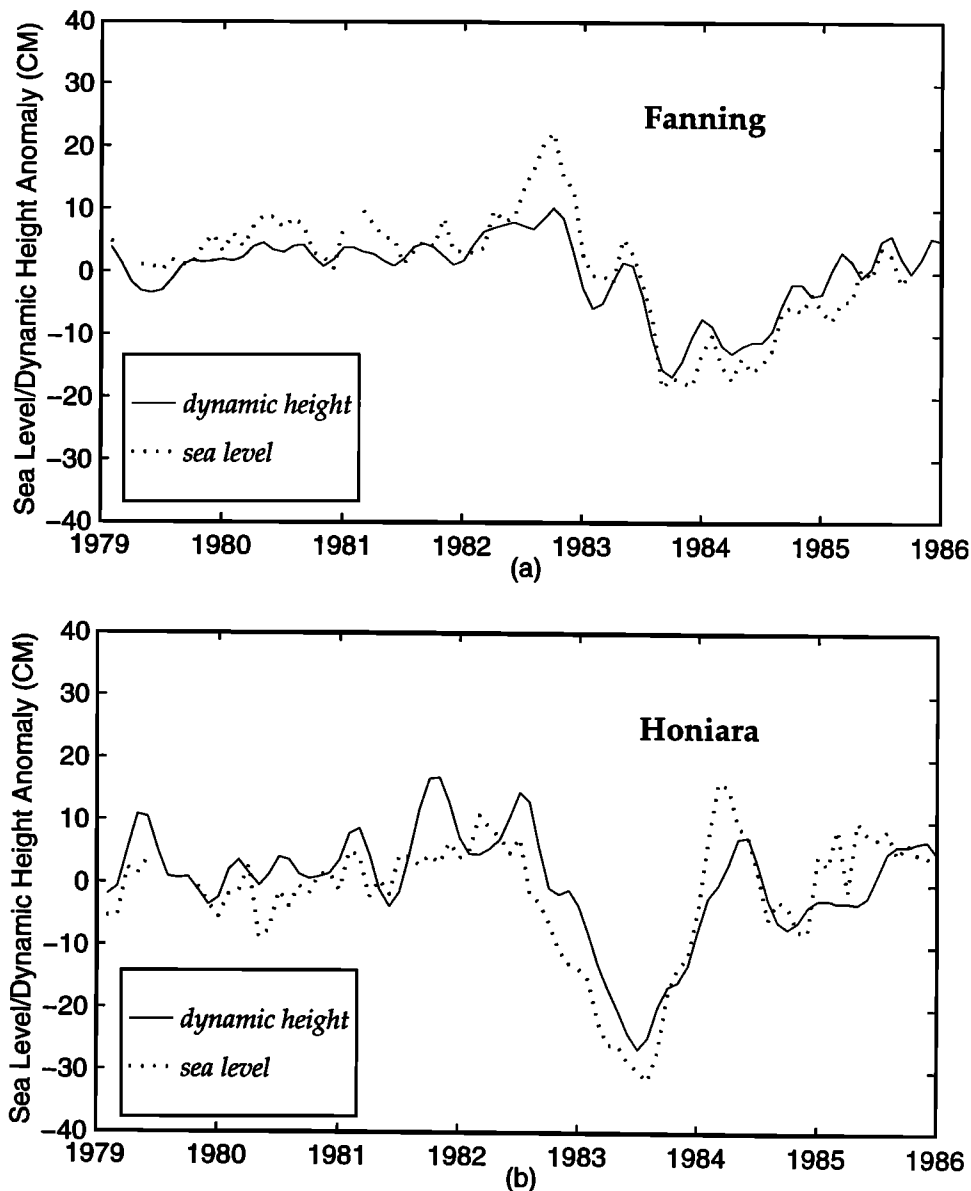
**Figure 2.** Comparison of dynamic height data with sea level stations at nearby locations for stations (a) Fanning and (b) Honiara.

data and the dynamic heights reconstructed from four EOFs were 2.0 dynamic centimeters (dyn. cm) in the western and central sections and 1.0 dyn. cm in the eastern section. The error variances of the EOF amplitudes were estimated by assuming that the along-track correlation of errors was Gaussian with 4° decorrelation scale. Error variances of the EOF amplitudes for each of the three tracks are shown in Table 1.

## 4. The Model Error

Equation (2) shows that in the case without updating, the error covariance $\mathbf{P}$ is determined entirely by the matrices $\mathbf{L}$ and $\mathbf{Q}$ which determine the evolution of the state according to the dynamical model and the system noise covariance, respectively. $\mathbf{Q}$ must be estimated

from assumptions about the statistics of the model error. Here, as in MC, we assume that the system noise is dominated by errors in the forcing field. Two statistical models of the wind stress error are formulated. In the first the errors are assumed to be white in time and to have homogeneous anisotropic Gaussian covariance structure; that is, if the forcing error is given by $e(x, y, t)$, then the forcing error covariance is assumed to have the form

$$\langle e(x_0, y_0, t_0)e(x_1, y_1, t_1)\rangle = \sigma^2$$
$$\cdot \exp[-(x_1 - x_0)^2/L_x^2 - (y_1 - y_0)^2/L_y^2]\delta(t_1 - t_0) \quad (6)$$

where $\sigma$, $L_x$, and $L_y$ are constants. In the second we assume that the forcing error variance $\sigma^2$ is a nonconstant function of $x$ and $y$. The covariance of the forcing errors at the points $x_0, y_0$ and $x_1, y_1$ then has the form
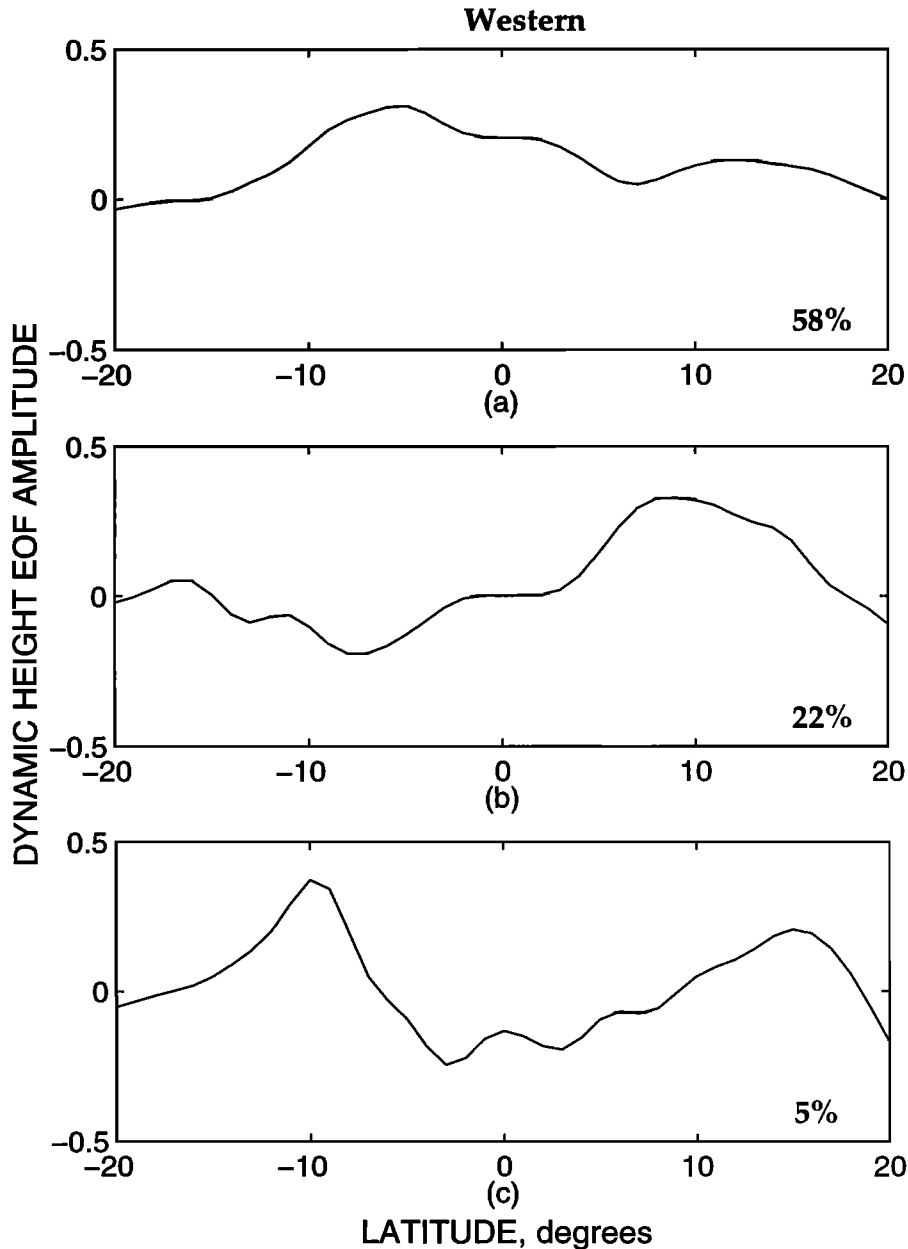
**Figure 3.** Empirical orthogonal functions (EOFs) of interannual dynamic height variability along the three tracks shown in Figure 1. Percentage of total variance accounted for by each EOF is shown in the bottom right. (a)–(c) Leading EOFs for the western track. (d)–(f) Leading EOFs for the central track. (g)–(i) Leading EOFs for the eastern track.

$$\langle e(x_0, y_0, t_0) e(x_1, y_1, t_1) \rangle = \sigma(x_0, y_0) \sigma(x_1, y_1)$$
$$\cdot \exp[-(x_1 - x_0)^2 / L_x^2 - (y_1 - y_0)^2 / L_y^2] \delta(t_1 - t_0). \quad (7)$$

In the experiments shown here we set $L_x = 10°$ and $L_y = 4°$. This differs from the value $L_y = 2°$ used in MC. In dissipative systems such as this one, the filter can be iterated according to (2) without updating until **P** reaches a steady state. This calculated **P** can be used to form an a priori estimate of the forecast errors of the model without assimilation, which may then be compared to statistics calculated from the actual differences between the forecast and observed sea levels. When this is done with **Q** determined from (6) with

$L_y = 2°$ as in MC, the result is a serious overestimate of the variances of the error at Yap, Truk, and Kwajalein in the northwest part of the domain. This can be understood in terms of the dynamical model. Away from the equator, a significant portion of the sea level height anomaly is due to the local effect of wind stress curl. This is not well represented by the truncated expansion in wave modes used in the earlier model. A simple calculation shows that the expected variance of $-\tau_y^{(x)}$ is inversely proportional to the square of the meridional decorrelation length. Table 1 of MC shows that wind stress error distributions with 3 and 4° meridional correlation lengths fit the observed error covariances nearly
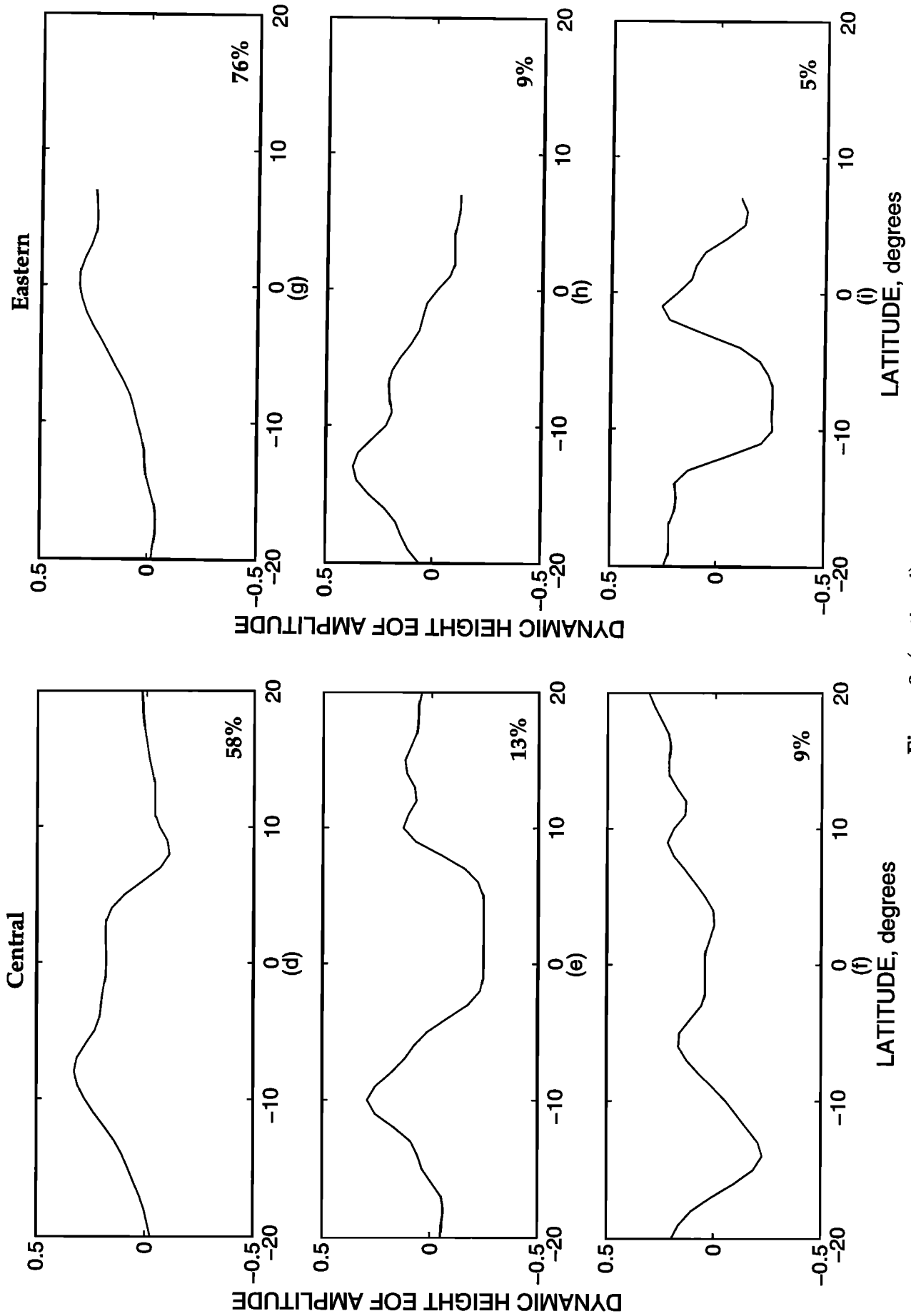
Figure 3. (continued)

**Table 1.** Error Variances of Observed Dynamic Height Empirical Orthogonal Functions

| EOF | West, $cm^2$ | Center, $cm^2$ | East, $cm^2$ |
|---|---|---|---|
| 1 | 43.9 | 38.1 | 50.5 |
| 2 | 39.2 | 31.5 | 49.6 |
| 3 | 30.8 | 29.7 | 31.4 |
| 4 | 23.5 | 23.3 | 21.6 |

Observational errors are assumed to be white in time and to have variances of 6.7, 6, and 8 $cm^2$ for the western, central, and eastern tracks, respectively. Observation error covariances were assumed homogeneous in latitude, with Gaussian shape and width of 4°. Errors in observations from different tracks were assumed to be independent. Numbering from top to bottom proceeds in descending order of proportion of total variance.

as well as the chosen distribution with a 2° decorrelation length.

In the earlier work with the simple model, the choices of $L_x$ and $L_y$ were based on comparison between the estimated forecast error covariance matrix and the sample covariance matrix, i.e., the covariance matrix calculated directly from the differences between forecast and observed sea level height. The criterion for comparison between the two matrices was a weighted sum of the squared differences between the lead EOFs. In the earlier work, with the wave model and data confined to near-equatorial tide gauge stations, the EOFs of the sample covariance matrix were consistent with those of the estimated error covariance matrix. This was not the case in the experiments with the CP model. Given this discrepancy with the results from MC, we set out to investigate whether a reasonable estimate of the observation error covariance matrix could be constructed with 8-year time series. A given covariance matrix was used to generate white time series of limited length, in our case, 8 years of artificial data at 1-month intervals. We then used the resulting time series to attempt to reconstruct the covariance matrix used in its generation. The result was that an 8-year, 15-channel monthly white time series is not long enough to reconstruct faithfully the covariance matrix used to generate it.

From repeated experiments following this procedure, with different prior covariance matrices and different seeds in our random number generator, we learned that different realizations of stationary white sequences with the same covariance matrices can be very different from one another, and simply summing squares and cross products yielded a very poor approximation of the underlying covariance matrix. Comparing a matrix of sums of squares and cross products of an 8-year, 15-channel time series to a set of theoretically derived alternatives is therefore not fruitful.

Because of the greater applicability of the CP model, there were more stations available for comparison in the present work than in the previous. Unlike the earlier work, a reasonable picture of the model error characteristics could be deduced from the error variances.

The matrix $\mathbf{Q}$ for the homogeneous model was calculated from a Monte Carlo simulation based on homogeneous Gaussian error covariance, with zonal and meridional scales of 10° and 4°, respectively, and an initial value for the total wind stress error variance of $(\rho_a/\rho_w)^2 C_D^2 \times 434(m^2s^{-2})^2$ (where $C_D$ is the drag coefficient, here taken to be 1.5, $\rho_a$ is the density of air, and $\rho_w$ is the density of water), 75% of the value used in MC. In our first rough comparisons this value gave rise to better error estimates than the original MC value. We attribute the better fit with the smaller error variance to the more efficient quadrature scheme in CP. As in MC, the drag coefficient was given by $\rho_a C_D = 1.95 \times 10^{-3}$.

For each trial of our Monte Carlo procedure we generated a Gaussian random wind field with covariance given by (6). This random field was used to drive the model for a single time step, given zero initial conditions. The covariance of the collection of single-step model outputs from trials conducted this way was taken as our value of $\mathbf{Q}$.

Our inhomogeneous error model was constructed by a Monte Carlo procedure similar to the one used to construct the homogeneous error model. We assumed a covariance function of the form given by (7), with the function $\sigma^2(x, y)$ calculated from the variance, point by point, of the fields of differences between the FSU and SAWIN cloud track wind analysis for the period 1979–1983.

The field of mean square differences between FSU and SAWIN was smoothed three times with a five-point smoother and normalized by 0.77 times the largest value of the resulting field. We arrived at the normalization factor of 0.77 through statistical comparisons, performed as follows: variances of differences between the output of the CP model, driven by FSU winds following a year of spin-up time, and observations of sea level and dynamic height anomalies were calculated. Prior estimates of these variances based on the steady state value of the model error covariance $\mathbf{P}$ were also calculated. Since the evolution of $\mathbf{P}$ is a linear function of $\mathbf{Q}$, multiplication of $\mathbf{Q}$ by a scalar would have the ultimate effect of multiplication of the prior estimates of the variances by that same scalar. We found that multiplying $\mathbf{Q}$ by a factor of 0.77 gave the best agreement between the prior estimates of the variances and the variances themselves.

The result, shown in original normalized form in Figure 4 (i.e., prior to multiplication by 0.77), was then multiplied, point by point, by each randomly chosen wind error field in the Monte Carlo simulation. The major effect of this scaling operation is to reduce the estimated system noise variance to as little as 30% of its original value (i.e., the homogeneous value) at points where the FSU analysis and the cloud track winds are in close agreement and raise it as much as 25% where the two differ. It is not surprising that the smallest values for this field (i.e., regions where FSU and SAWIN agree most closely) are located along major ship tracks since the major source of data for the FSU analyses are ship winds collected along these routes. The values of
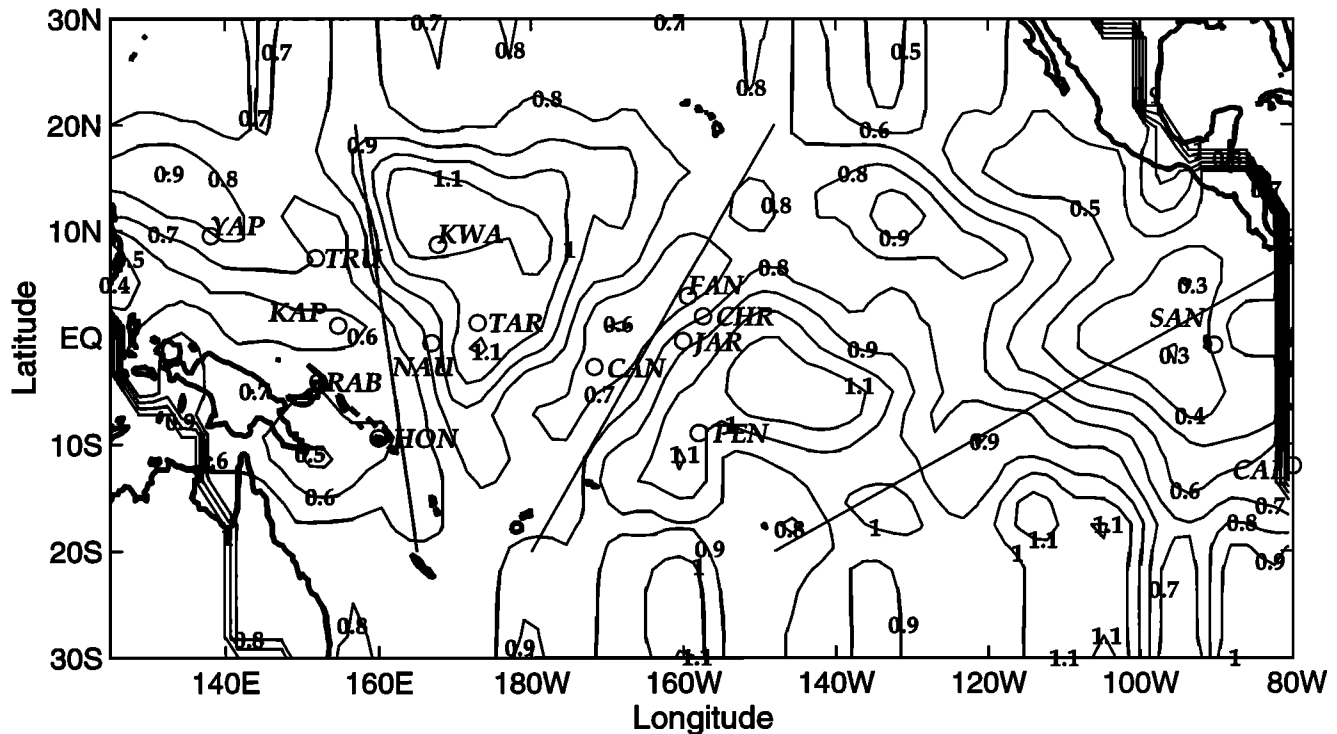
**Figure 4.** Normalized variance of the difference between the SAWIN and Florida State University (FSU) monthly mean windstress anomaly products. Abbreviations of island station names are YAP, Yap; TRU, Truk; KAP, Kapingamarangi; RAB, Rabaul; HON, Honiara; NAU, Nauru; KWA, Kwajalein; TAR, Tarawa; CAN, Canton; FAN, Fanning; CHR, Christmas; JAR, Jarvis; PEN, Penrhyn; SAN, Santa Cruz; and CAL, Callao.

$L_x$ and $L_y$ were the same as those used in the homogeneous model.

The results of our Monte Carlo calculations of the system noise variance **Q**, transformed to units of sea level height are shown in Figure 5. The quantities displayed as a contour map in Figure 5 are the square roots of the diagonal elements of the matrix $\mathbf{HQH}^\mathbf{T}$, where **H** is the matrix which transforms a model state vector into the corresponding map of sea level height anomalies. The homogeneous error model was multiplied by a factor of 0.84, determined by the same process used to normalize the inhomogeneous model.

The map of the inhomogeneous model system noise variance (Figure 5b) reflects the fact that regions where FSU winds differ from other wind products (SAWIN, in this case) are assumed to be regions in which the FSU product is less reliable, and therefore our estimate of the error is greater than regions in which different wind products agree. Comparison of Figures 5a and 5b shows that the inhomogeneous model has greater error assigned to regions away from the ship tracks, especially in areas east of Kwajalein, east of the Line Islands, and northeast of Penrhyn (see Figure 5c). Reduced error estimates correspond to areas where the FSU wind product is well sampled along ship tracks, namely, west of the western XBT track, east of 115°W, and near the Line Islands. With the factors for each type of model chosen as they were to minimize the differences between

the statistics of the (model output minus observation) time series and the prior estimate of that quantity, the mean difference between the two fields is close to zero.

The estimated variances of the differences between the predictions of the model without data assimilation and the observed tide gauge and XBT data are depicted in Figure 6 as a scatterplot against the actual variances of the differences between model output and observed tide gauge and XBT data. In a properly tuned model the points on the scatterplot should cluster about the line with unit slope. Since the scaling factors for both the inhomogeneous and homogeneous error models were calibrated beforehand to fit the best estimate of the model error, the points from both error models (plus symbols for homogeneous and asterisk symbols for inhomogeneous in Figure 6) straddle the line with unit slope. However, in every instance, errors derived from both models tend to underestimate the value of the error when the variance is large and overestimate it when it is small. Examples in which both error models do especially poorly include the tide gauge stations at Rabaul, Nauru, Fanning, and Callao, the northern and southern points along the XBT tracks, and the first two EOFs along the western track. For the homogeneous error model (plus signs in Figure 6) the model forecast error variance is usually greater than the corresponding forecast error variance for the inhomogeneous model. Exceptions occur in a band west of and including Pen-
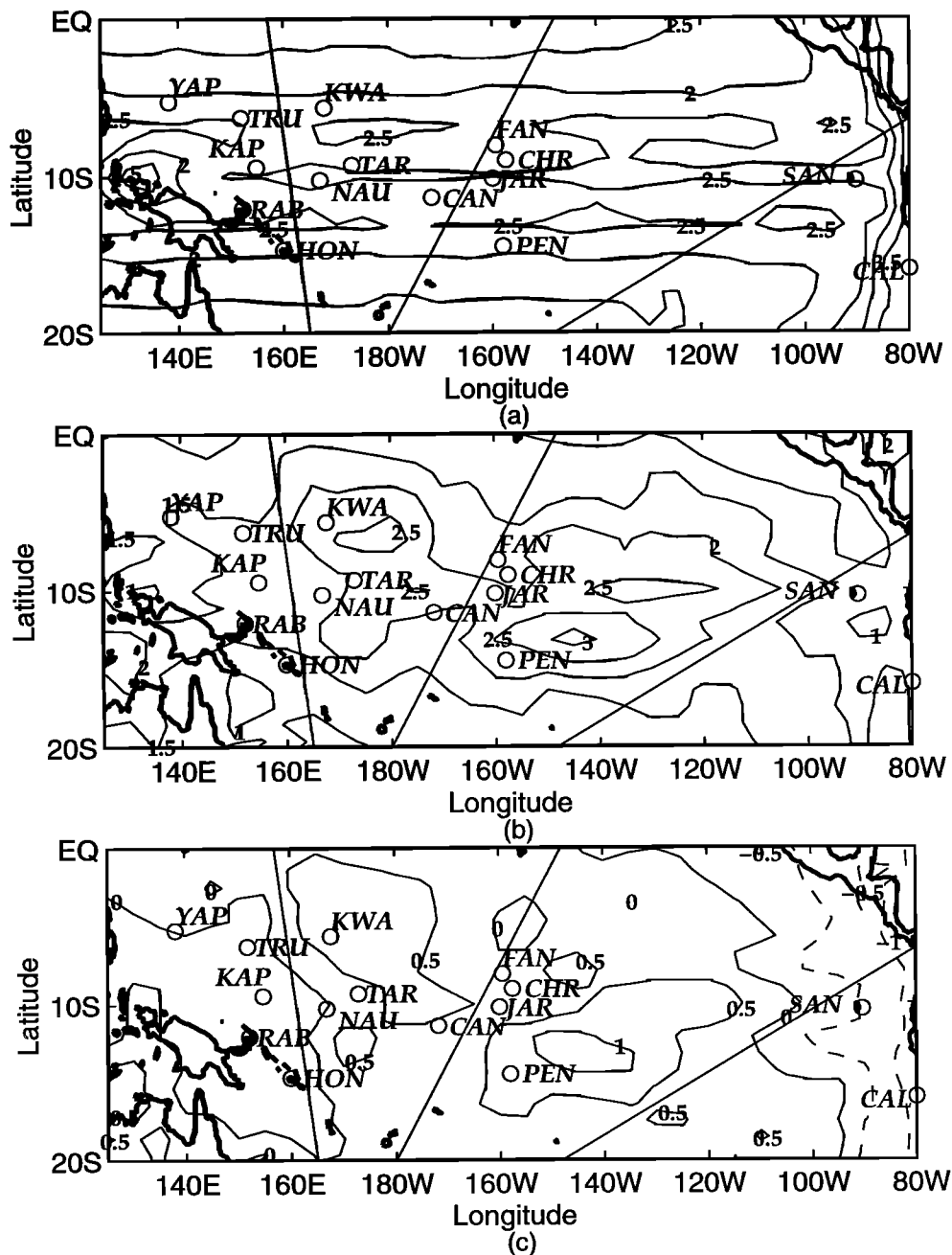
**Figure 5.** Root-mean-square (RMS) system noise variance, plotted as contribution to error in sea level height, in units of centimeters. This can be viewed as the square roots of the diagonal elements of the matrix $\mathbf{HQH^T}$, where $\mathbf{Q}$ is the system noise covariance (see section 2.2) and $\mathbf{H}$ is the matrix which maps the state vector into the gridded map of sea level height anomalies. (a) RMS system noise amplitude for the model with statistically homogeneous error variance. (b) Similar to Figure 5a, but with the noise variance distributed in space according to the distribution shown in Figure 4. (c) Difference field for inhomogeneous (Figure 5b) minus homogeneous (Figure 5a).

rhyn and north and west of Kwajalein. Visual inspection of these results alone yield no clear decision as to which model is better.

To quantify the comparison between the two models, the distance to the line with unit slope was calculated for each data point in Figure 6. The statistics for the mean and standard deviation of these distances are tab-

ulated for each panel in Figure 6. For each type of data except the EOFs (Figure 6c), mean (labeled MEAN) and the scatter (labeled STD) are greater for the homogeneous than for the inhomogeneous error model. This result indicates to us that the inhomogeneous error model does slightly better than the homogeneous error model in estimating the actual model errors, taken as a

whole. It is our opinion that the improvement of the error estimate near the eastern boundary (especially the tide gauge station at Callao) makes the inhomogeneous error model a better choice for further investigation.

Figure 7 shows maps of estimated RMS errors for the model, without updating, based on calculation of the steady state value of **P** by integration of (2) to equilibrium with **Q** derived from the homogeneous and inhomogeneous wind error models. While the maps shown in Figure 5 represent the errors assumed to be introduced into the model analysis at each step, the maps shown in Figure 7 represent the cumulative effect of these errors on the model output.

The structure of the two fields represented in Figures 7a and 7b exhibit differences which might have been expected. The greatest differences are in the northwest, where wind observations are fairly dense and the

model is expected to be fairly good, and in the eastern part of the basin off the equator, where the observations are sparse. The magnitudes of the differences, however, are small; the RMS error maps differ by less than 1.0 cm throughout the model region. The mean difference between inhomogeneous and homogeneous error model results is approximately -0.4 cm (see Figure 7c), well within the error tolerance for the observations themselves. It is surprising, but apparently true, that the equilibrium value of **P** calculated from (2) is not very sensitive to spatial inhomogeneities in the statistical model of forcing errors. For the present purpose, the choice between the system noise covariance matrices derived from inhomogeneous and homogeneous forcing error models is a matter of indifference. For the remainder of this study we use the inhomogeneous model. The error estimates are more reliable near boundaries, and
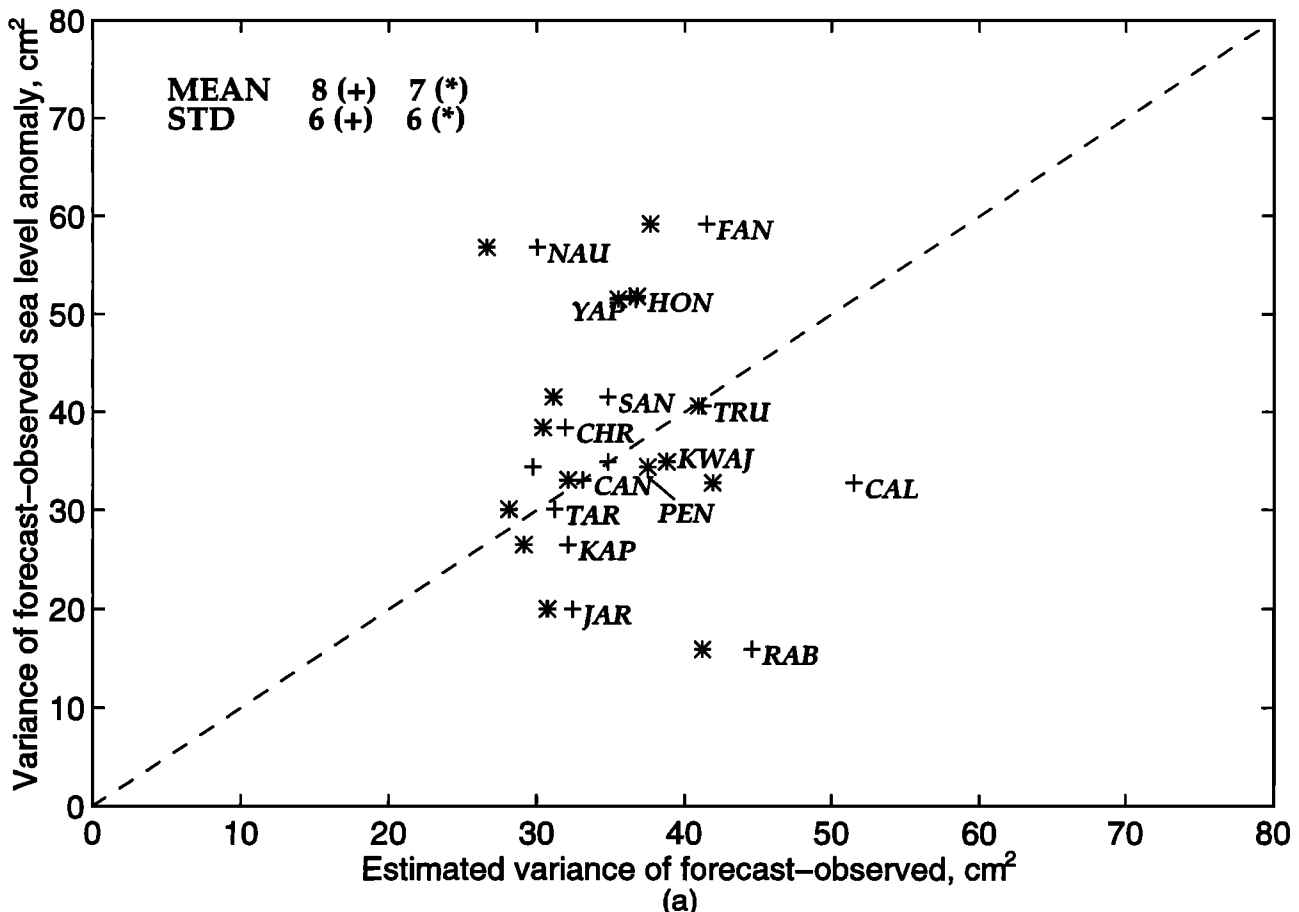


**Figure 6.** Comparison of homogeneous and inhomogeneous error models. Variances of time series of differences between observations and wind-driven model output with no assimilation for homogeneous (pluses) and inhomogeneous (asterisks) error models are assigned to the ordinate axis. Values on the abscissa are prior estimates of the variances of model output minus observation based on **P** at the end of 1985. (a) Scatterplot of variances of model minus observation time series versus prior estimates of same for 15 island stations. Estimated variance is shown on the abscissa. Points corresponding to each island have the same ordinate, so labels are omitted from all but one set of points for clarity. The line with unit slope is plotted for comparison. (b) Same as Figure 6a, but for 26 dynamic height values, chosen at 5° intervals along the 3 XBT tracks. (c) Same as Figure 6a, but for the leading four EOF amplitudes for each of the three XBT tracks. Values corresponding to the mean distance from each point in the scatter to the line with unit slope (MEAN) and the standard deviation about that mean (STD) for each of the two error models are tabulated in each frame.
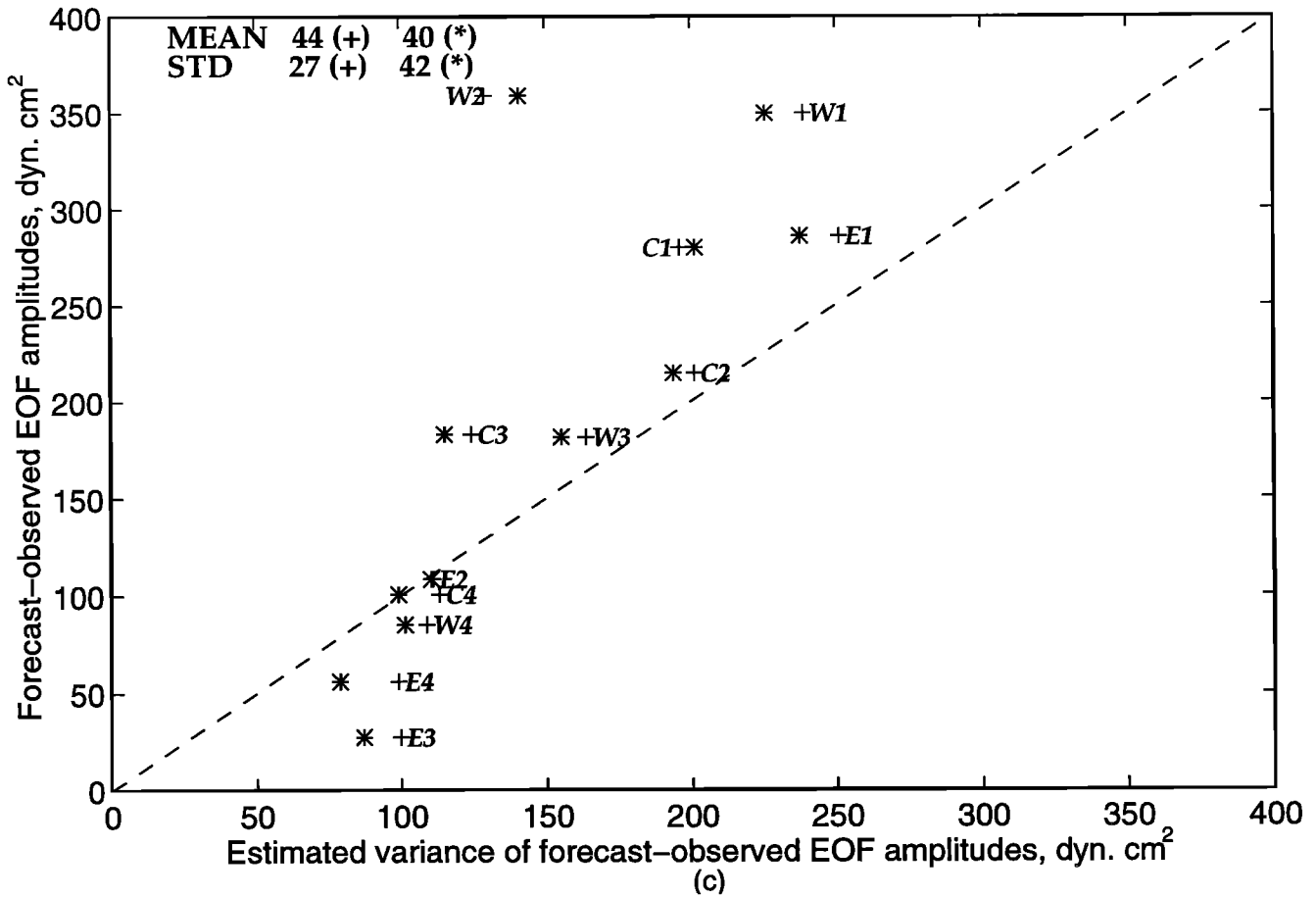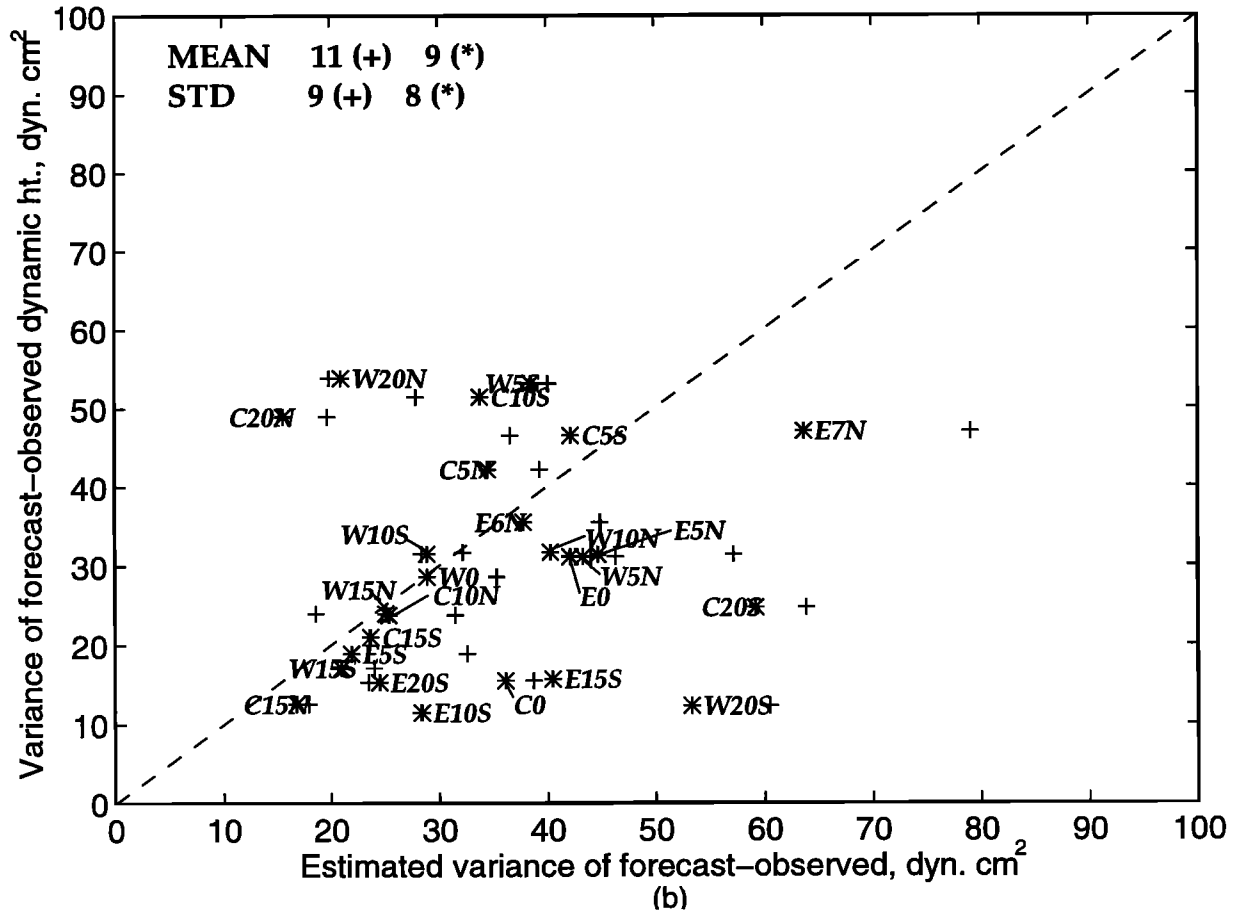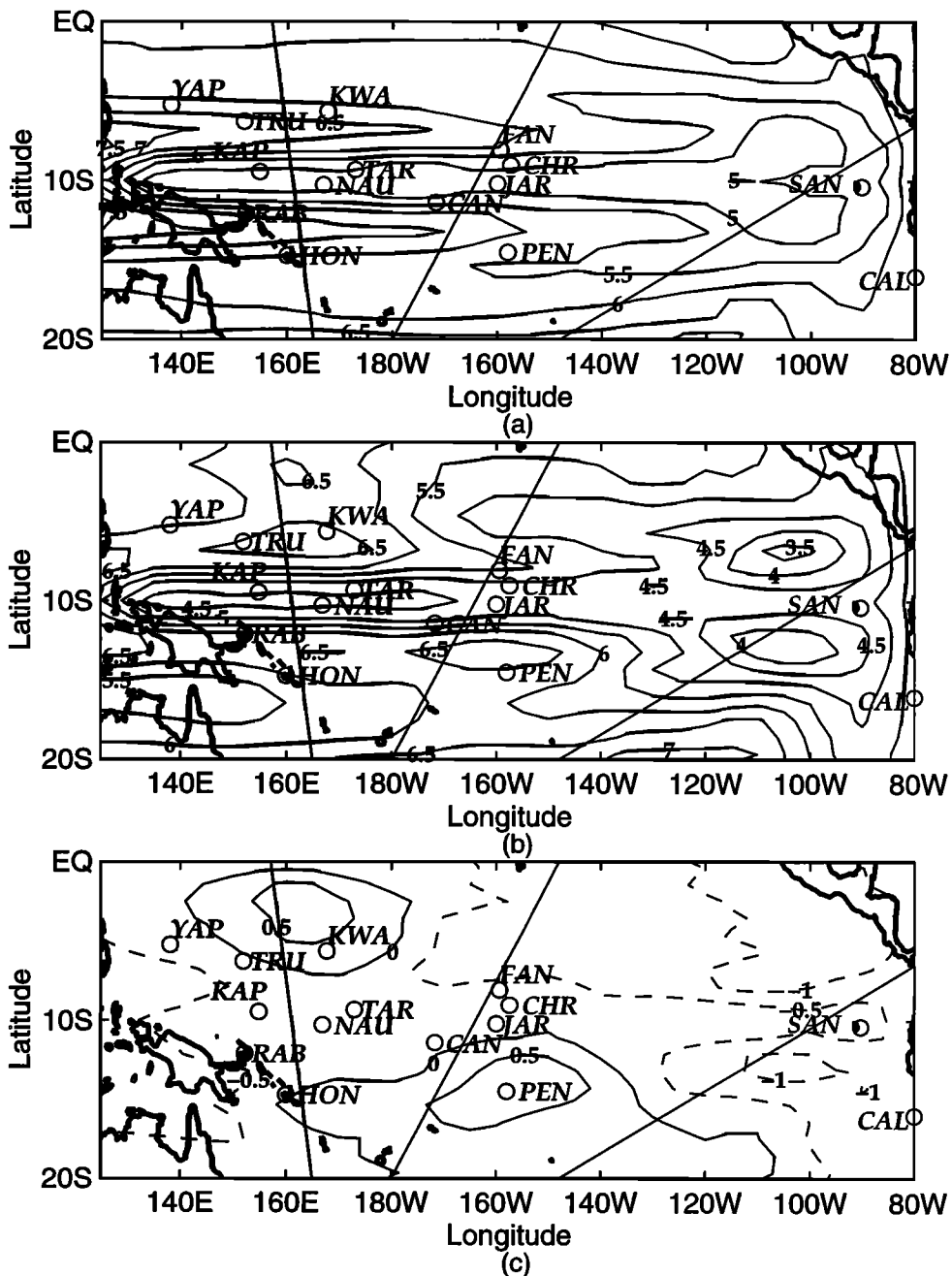
(b)



(c)

**Figure 6.** (continued)

**Figure 7.** Maps of estimated RMS error in sea level height anomaly for model without assimilation. These maps are based on the evolution of the error covariance according to the dynamical model after 8 years of integration. The model is closest to dynamical equilibrium at the equator and is still evolving significantly poleward of about 15°. Contours are in centimeters. (a) RMS sea level height error based on homogeneous wind error model. (b) RMS sea level height error based on inhomogeneous wind error model. (c) Difference field for inhomogeneous (Figure 7b) minus homogeneous (Figure 7a).

we believe it to be a more faithful representation of reality, even though the large-scale effect on the estimated errors in sea level variation at most stations is small.

## 5. Results

### 5.1. Baseline Comparisons

This is an application in which we expect data assimilation to be useful for both descriptive and analytical purposes. The data themselves are too sparse to provide comprehensive analysis on their own, and simple objective analysis schemes are not constrained to produce physically consistent results. Simple models capture many of the important dynamical features of the physical system, but the data are too sparse to provide them with adequate forcing and initialization fields.

With the available forcing fields for this period the model by itself does not capture the observed signal variance. Of course, the total signal variance could be

increased by artificially increasing the drag coefficient. *Sheinbaum and Anderson* [1990] found that by increasing the drag coefficient, they improved the comparison of XBT data to a model similar to ours driven by FSU winds for 6 months in 1980. Their results, unfortunately, are not directly comparable to ours since they did not remove the seasonal cycle as we did. They found that the major effect of increasing $C_D$ was to increase the thermocline slope; a similar effect was obtained by decreasing the stratification, as expected from dynamical considerations. It is possible that the apparent bias in the direction of weaker winds in the FSU data set is due to the smoothing applied to the data in the construction of the data set and the processing of the FSU wind fields for this study.

It would be difficult to justify an increase of more than about 50% in $C_D$ on physical grounds. The improvement would be greatest east of about 160°W, but the amplitude would still be deficient, judging by the results of the experiment without assimilation. The results at Kapingamarangi and Tarawa in the western equatorial region, where the El Niño-Southern Oscillation (ENSO) response is of the proper amplitude, would be worse.

As a first step in the assessment of the impact of data assimilation on the model output, we compare the variability of the model sea level anomaly with an objective analysis formed from in situ observations. Figure 8 shows the RMS sea level height anomaly for the model run with no data assimilation and for a time series of maps generated by statistical objective analysis based on all of the available data. The sea level height anomaly was mapped by standard objective analysis techniques, with zonal and meridional decorrelation lengths of 15° and 3°, respectively, as described by *Meyers et al.* [1991]. XBT data were treated as being identical to tide gauge data for the purpose of this analysis. *Meyers et al.* [1991] showed that the mapping is not very sensitive to the particular parameter choice. Figures 8a and 8b exhibit similar general patterns. The model output is too weak in data-dense regions, especially in the east and southwest portions of the domain.

The sparseness of the data prevents us from seeing a uniformly accurate picture of the signal amplitude in the objective analysis. In data-poor regions the objective analysis is no stronger than the model output. Figures 8a and 8b also differ in the eastern part of the basin, where the structure of the waveguide and the broadening of the contours toward the east due to the meridional scale of the reflected Rossby waves are apparent in the model output but not in the objective analysis.
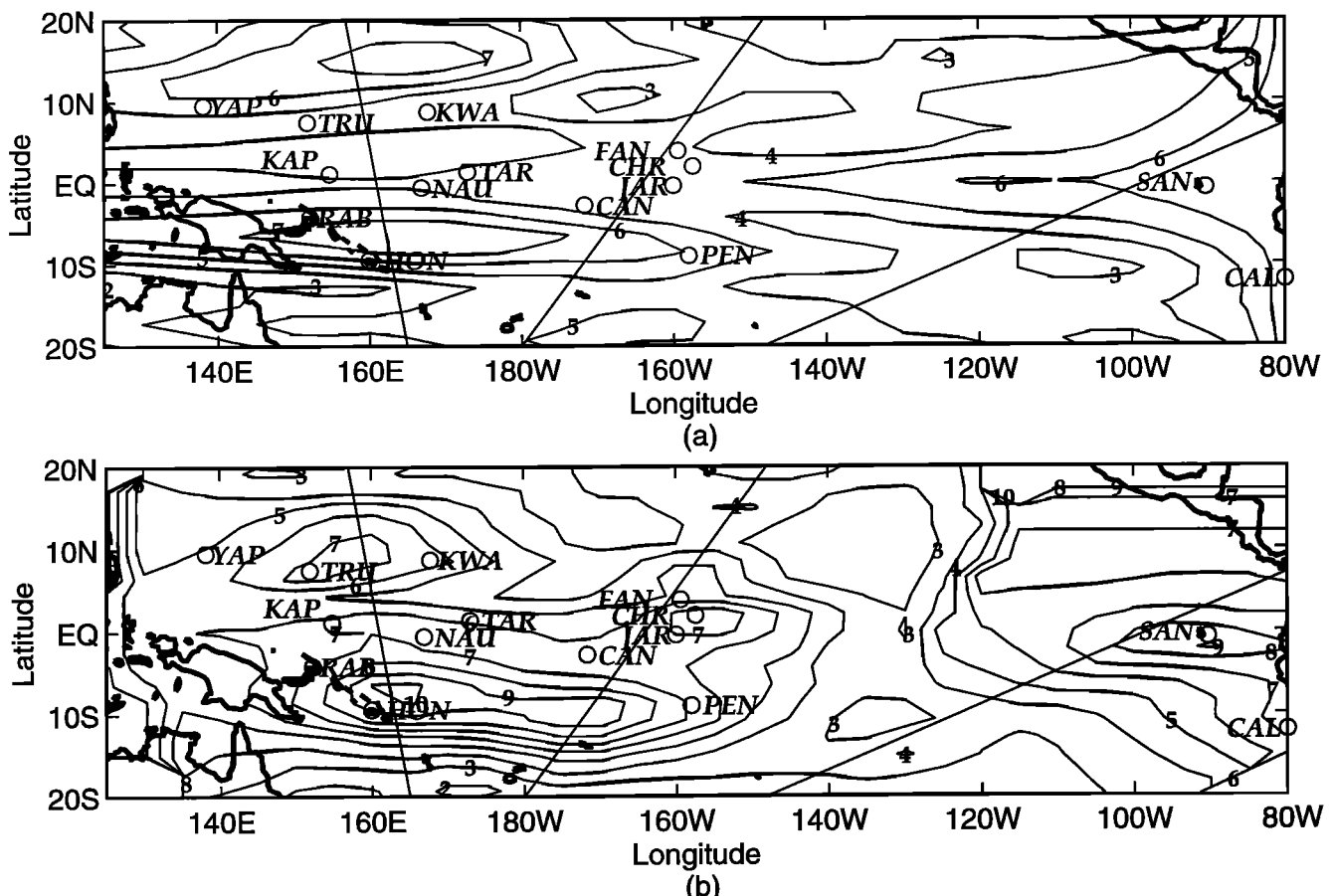


**Figure 8.** Maps of RMS sea level height anomaly in centimeters, based on (a) 8 years of wind-driven model output, with no data assimilation and (b) objective mapping of all available data for that period.
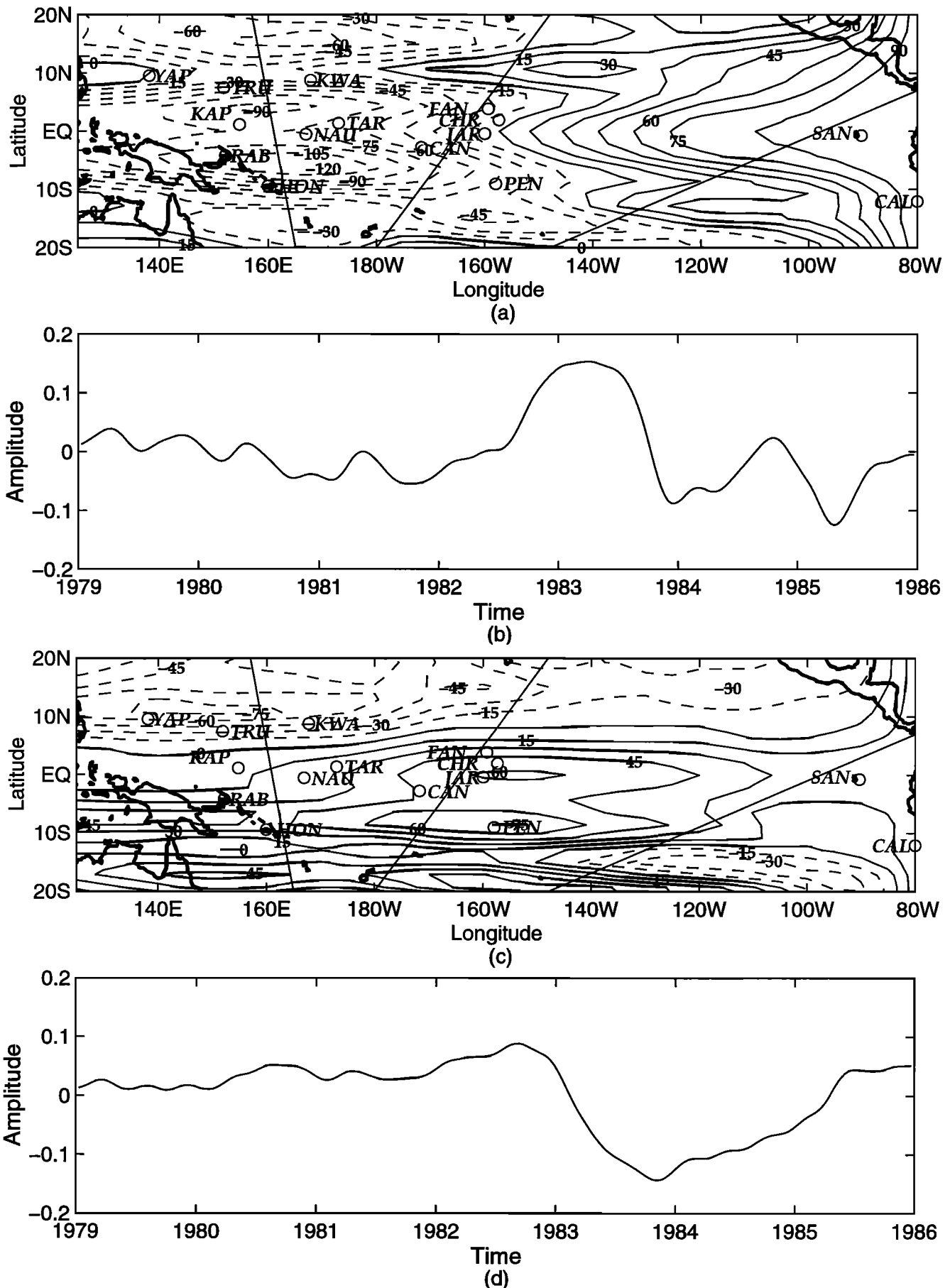
**Figure 9.** Spatial structure and time series of EOFs of the sea surface height anomaly produced by the wind-driven model without data assimilation. (a) Contour map of leading spatial mode, accounting for 40% of the total signal variance. (b) Model time series of amplitudes of the mode shown in Figure 9a. (c) Same as Figure 9a, but for second leading spatial mode, accounting for 20% of the total signal variance. (d) Same as Figure 9b, but for second leading spatial mode.

In order to examine the large-scale spatial structure of the dynamic topography anomaly field, EOFs were calculated from the model output and corresponding EOFs were calculated from the XBT data, with dynamic height anomaly considered identical to surface height anomaly, and from surface height anomaly data from Rabaul, Truk, Kwajalein, Penrhyn, Fanning, Christmas, Santa Cruz, Kapingamarangi, Tarawa, and Canton. The island stations were selected for relative freedom from temporal gaps. Figure 9 shows the first two spatial EOFs of the model output, along with the time series of their amplitude. These EOFs together account for 60% of the variance of the model output field. The time series of amplitudes (Figures 9b and 9d) indicate that these EOFs carry the ENSO signal.

Figure 10 shows a mapped representation of the EOFs of the selection of data used to generate Figure 8b. These EOFs taken together account for 74% of the variance of the data selected. The spatial pattern of the lead EOF is qualitatively similar to the leading model EOF. Detailed differences may well reflect the spatial

sampling of the data which participate in the calculation. This EOF contains a greater proportion of the total variance than does its counterpart in the model output, but some of this may be due to the restricted number of degrees of freedom. The time series of amplitudes is dominated by the large ENSO event to an even greater extent than the model EOF amplitude.

The second data EOF is also similar in general pattern to the model EOF. The data and model EOFs represent about equal proportions of the total variance. It is therefore interesting that the data EOF amplitude exhibits a stronger response during the ENSO event of 1982–1983 than does the model EOF.

The reader should bear in mind that the maps shown in Figure 10 actually represent EOFs of data at irregularly spaced points. An objective mapping routine was used to generate the gridded fields from which Figures 10a and 10c were contoured. Details of the mapped structure in data voids are therefore to be viewed with suspicion; see, especially, the sign change in the region between the Galapagos ($\approx 90°$W) and the Line Islands
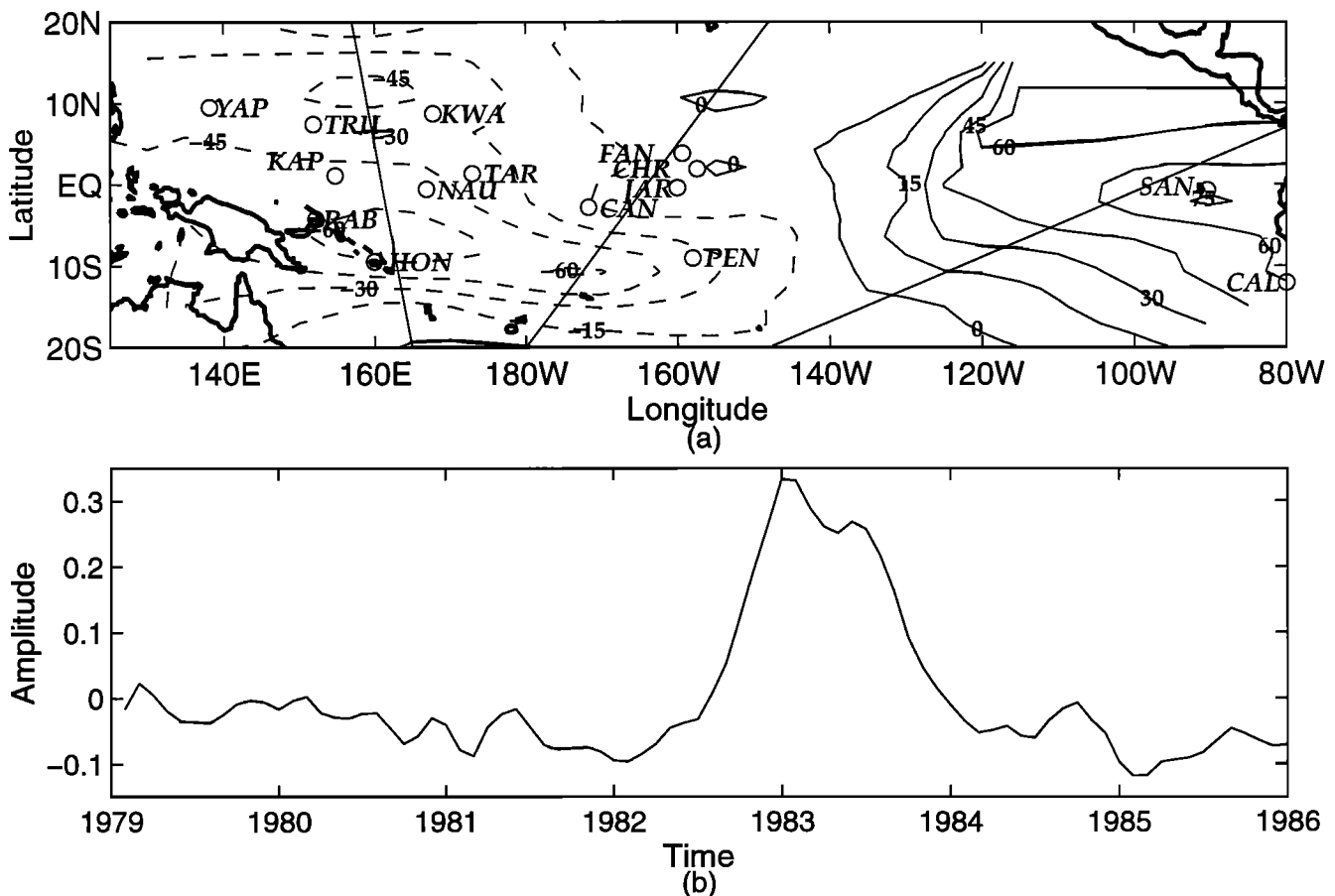


**Figure 10.** Same as Figure 9, but for time series of objective maps based on XBT data and tide gauge data at Rabaul, Truk, Kwajalein, Penrhyn, Fanning, Christmas, Santa Cruz, Kapingamarangi, and Tarawa. (a) Contour map of leading spatial mode, accounting for 52% of the signal variance. (b) Time series of amplitudes of the mode shown in Figure 10a. (c) Same as Figure 10a, but for second leading spatial mode, accounting for 22% of the total signal variance. (d) Similar to Figure 10b, but for second leading spatial mode.
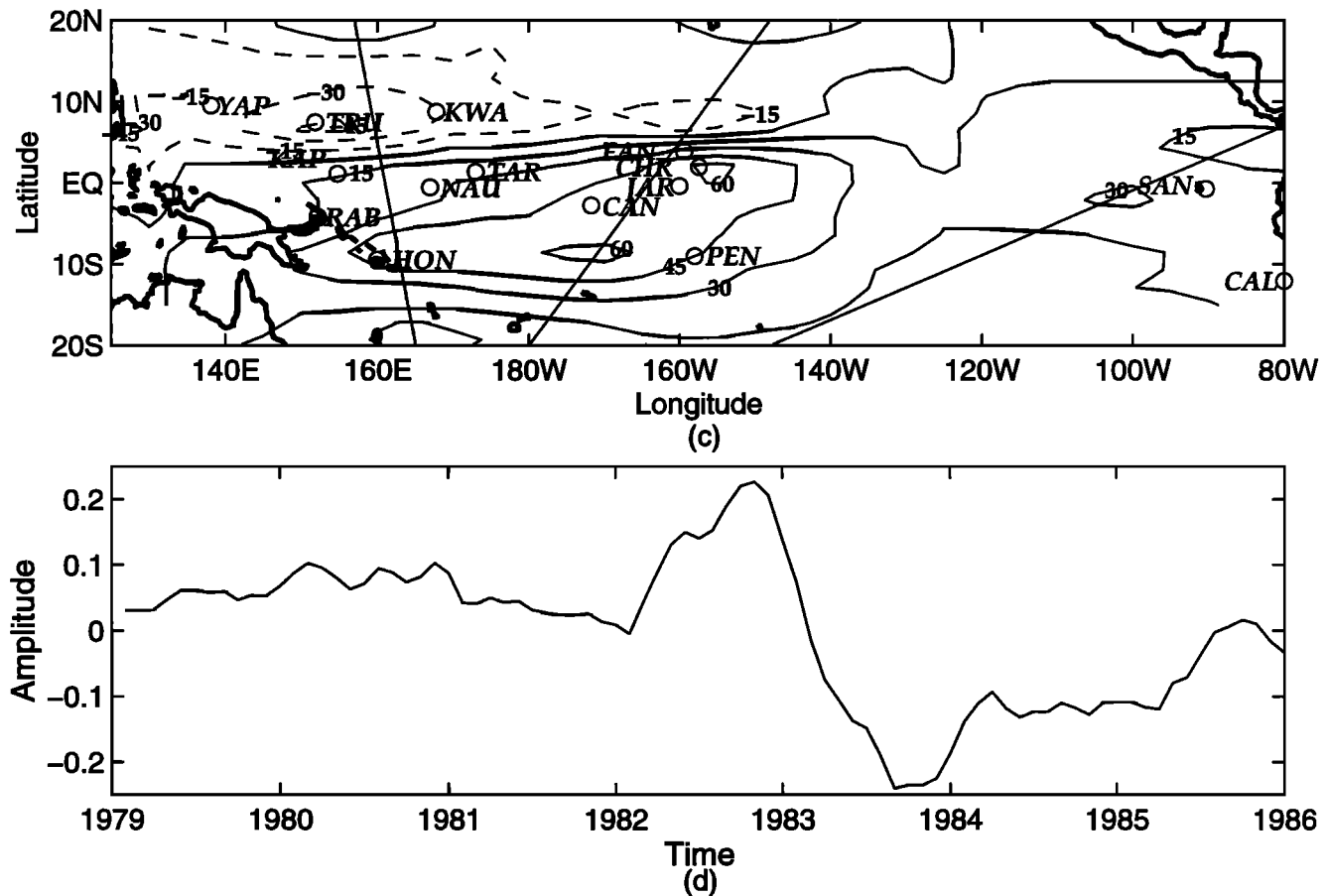
**Figure 10.** (continued)

($\approx 160°$W) in Figure 10a and the difference between Figures 9c and 10c in the northeast. The ENSO signal is more conspicuous in the second EOF than in the first.

### 5.2. Data Assimilation Experiments

Three data assimilation experiments were performed, all using the inhomogeneous form of $Q$, as follows: one in which data from a selection of tide gauges were assimilated (denoted as "ISL"), one in which the four leading EOFs of the XBT data were assimilated (denoted "XBT"), and, finally, one in which both tide gauge data and XBT data were assimilated (denoted "ISL+XBT"), respectively. We refer to the run without data assimilation as "NODA."

In all three assimilation runs the total variance of the height field was enhanced significantly as compared to NODA, approaching the total variance of the data. Maps of RMS amplitudes of the output of the data assimilation experiments are shown in Figure 11. Differences between the RMS amplitudes of the sea level height fields from the runs with data assimilation and the one without are shown in Figure 12. The overall patterns of the variance maps change very little. The greatest change is in the amplitude. It is noteworthy that all of the assimilation experiments had greater variance at every point than the experiment without assimilation.

EOFs of the sea surface height variability for the three assimilation runs are shown in Figure 13. The greatest effect of the assimilation process on the lead EOF is in the northwestern part of the basin, where the assimilation process has smoothed out the strong meridional gradient near $7°$N which extends from the western boundary nearly halfway across the basin in Figure 9a, the corresponding EOF for experiment NODA. In this respect the maps shown in Figures 13a, 13e, and 13i more closely resemble the corresponding data EOF (Figure 10a) than they do the model EOF without assimilation (Figure 9a). The corresponding gradient in the southwest remains strong in the assimilation runs as in NODA, though it is weakened slightly in XBT and XBT+ISL, where data from the western XBT track are influential. East of the date line, the leading EOFs from the assimilation runs resemble that from NODA, shown in Figure 9a, more closely than they do the leading data EOF shown in Figure 10a. The impact on the second EOF is not so obvious.

Variances of differences between estimated and observed quantities, along with estimates of these statistics based on covariance calculations performed in the filtering process are shown in Table 2. Estimates of observation error variances (i.e., the diagonal of $R$ from the Kalman filter formulation; see section 2.2) were added to the estimated error variances of the observed
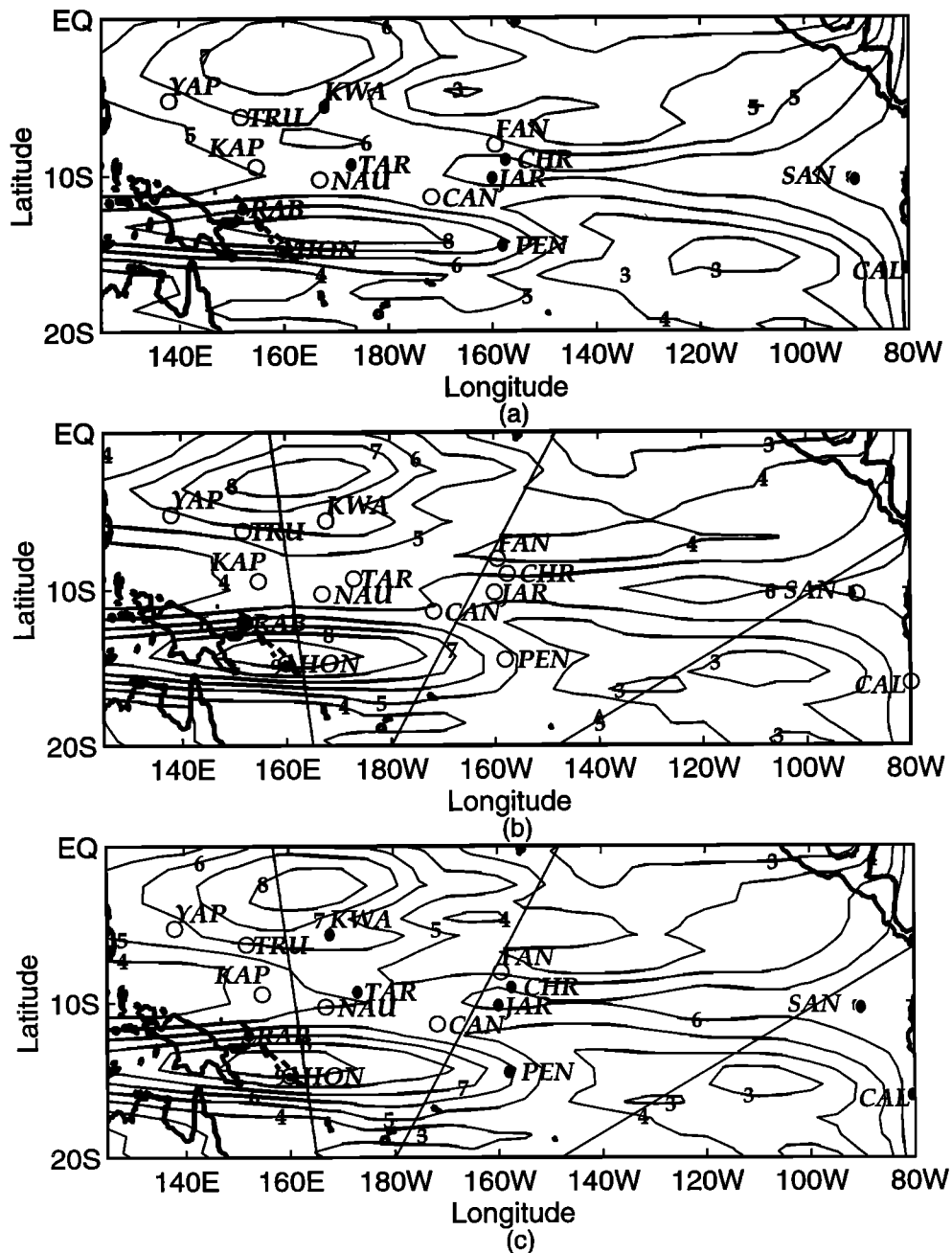
**Figure 11.** RMS signal amplitudes (in centimeters) for the three data assimilation runs. Solid circles denote tide gauge stations at which data were assimilated. Open circles denote tide gauge stations at which data were available but were not assimilated. (a) Experiment ISL, in which data are assimilated from tide gauges at Rabaul, Jarvis, Christmas, Santa Cruz, Tarawa, Kwajalein, Penrhyn, and Callao. (b) Experiment XBT, in which data are assimilated from the leading four EOFs of the XBT data in all three XBT lines. (c) Experiment XBT+ISL, in which data are assimilated from both tide gauges and EOFs of XBT data.

quantities in order to form estimates of comparable quantities, so the estimated variances of the differences between model output and observations for stations at which data were not assimilated are given by the diagonal elements of $MPM^T + R$, where $M$ is the matrix which maps the state vector into the vector of sea level heights, dynamic heights, and EOF amplitudes. The estimated error variances at stations from which data

were assimilated are given by the corresponding diagonal elements of $R - MPM^T$, as shown by *Miller* [1990]. These error estimates are based on the value of the state error covariance matrix $P$ after 8 years of evolution, with initial condition spun up for 6 years from the equilibrium $P$ from MC. This is very nearly at equilibrium near the equator; the departure from equilibrium increases in the poleward direction. This reflects the ex-
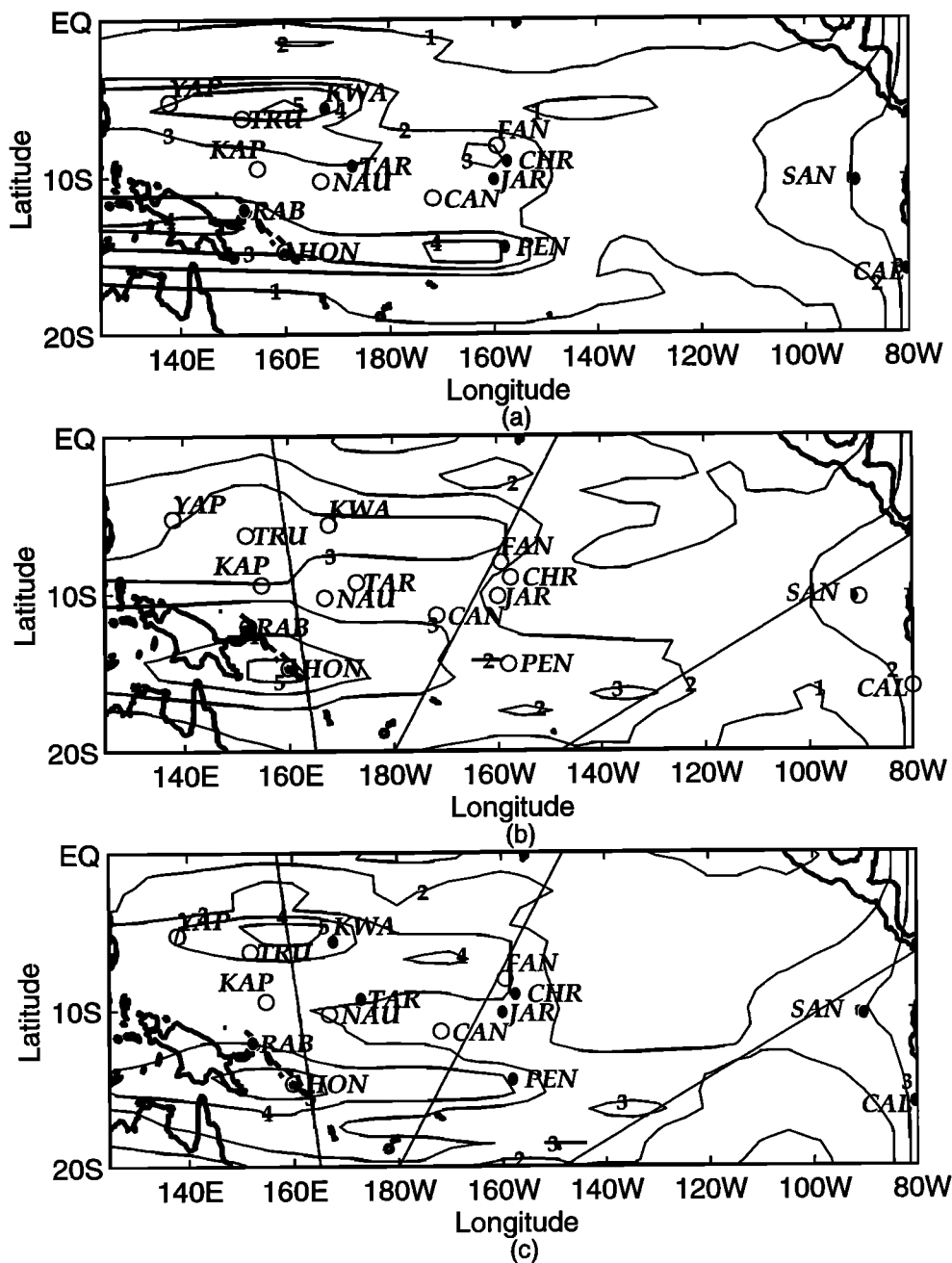
**Figure 12.** Differences between RMS signal amplitudes (in centimeters) for the assimilation runs and the run with no assimilation (NODA). Solid circles denote assimilation stations. Open circles denote stations at which data were available but were not assimilated. (a) ISL minus NODA, RMS amplitude of the tide gauge assimilation minus RMS amplitude of the model run without assimilation. (b) XBT minus NODA, same as Figure 12a, but for the XBT assimilation experiment. (c) XBT+ISL minus NODA, same as Figure 12a, but for the experiment in which both XBTs and tide gauges were assimilated.

tremely slow propagation of the high meridional mode Rossby waves which determine the state of the system away from the equator.

Most of the assimilation error estimates shown in Table 2 appear at least in the proper range. The major exceptions are the two lead EOFs in the western track. The error estimates for these quantities are distinctly overoptimistic. The consequence of this for the assim-

ilation process is that the model value will be given greater weight than it should have, while the data will be given correspondingly less. It is therefore surprising that the error estimates at the individual XBT locations are reasonably good, even in the west.

Errors are consistently overestimated at Rabaul, while they are consistently underestimated at Nauru, Fanning, Yap, and Honiara. The result at Fanning is
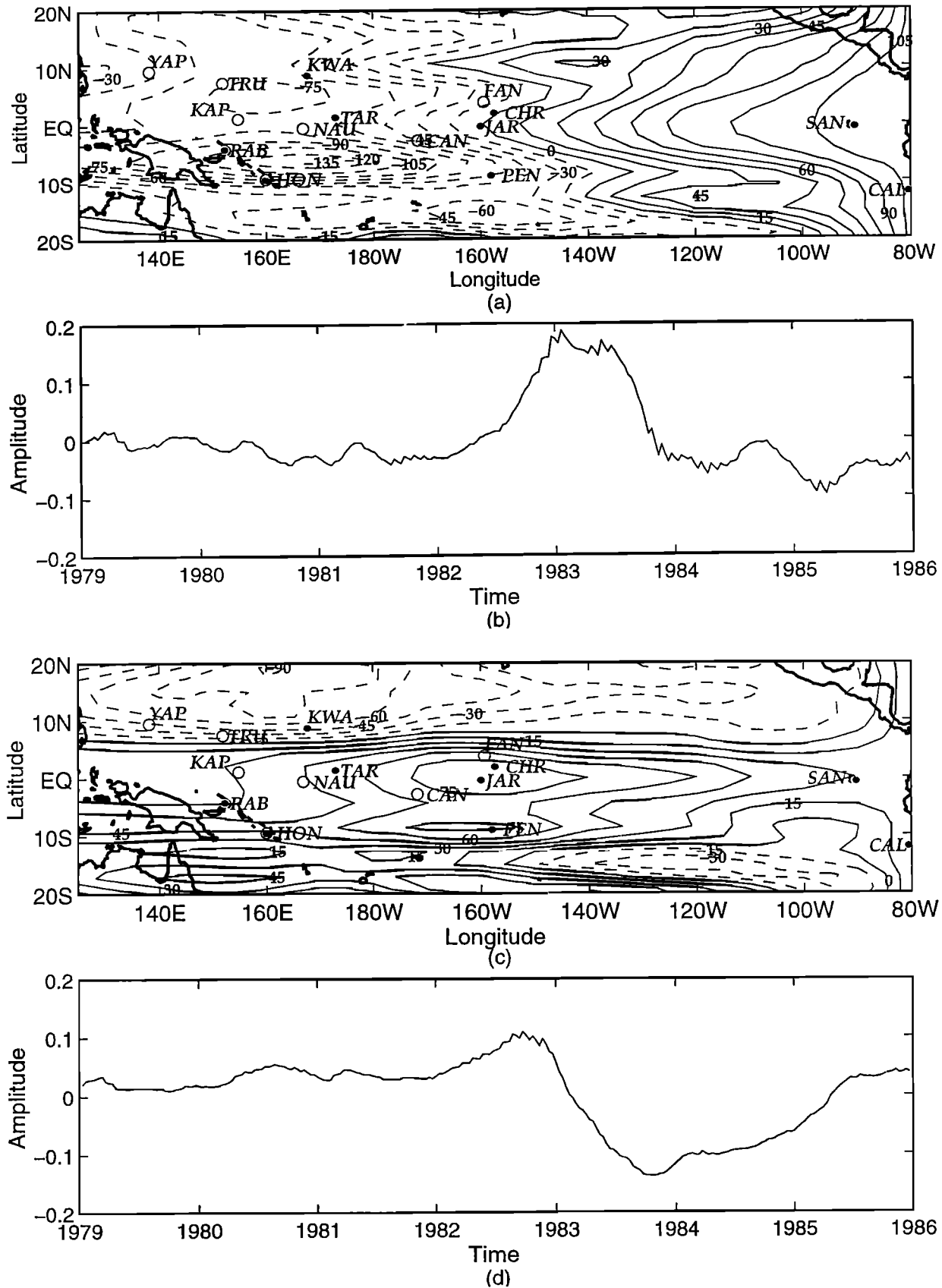
**Figure 13.** Empirical orthogonal functions of variability of sea level height for the three data assimilation experiments. (a) Lead spatial mode for experiment ISL. (b) Time series of amplitudes of the mode shown in Figure 13a. (c) Same as Figure 13a, but for second leading mode. (d) Same as Figure 13b, but for second leading mode. (e)–(h) Same as Figures 13a–13d, but for experiment XBT. (i)–(l) Same as Figures 13a–13d, but for experiment XBT+ISL.
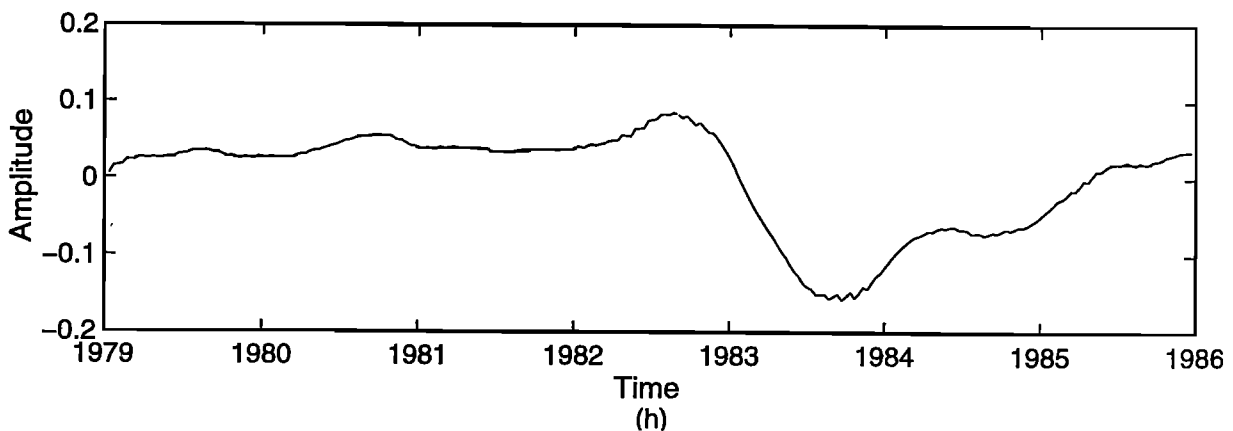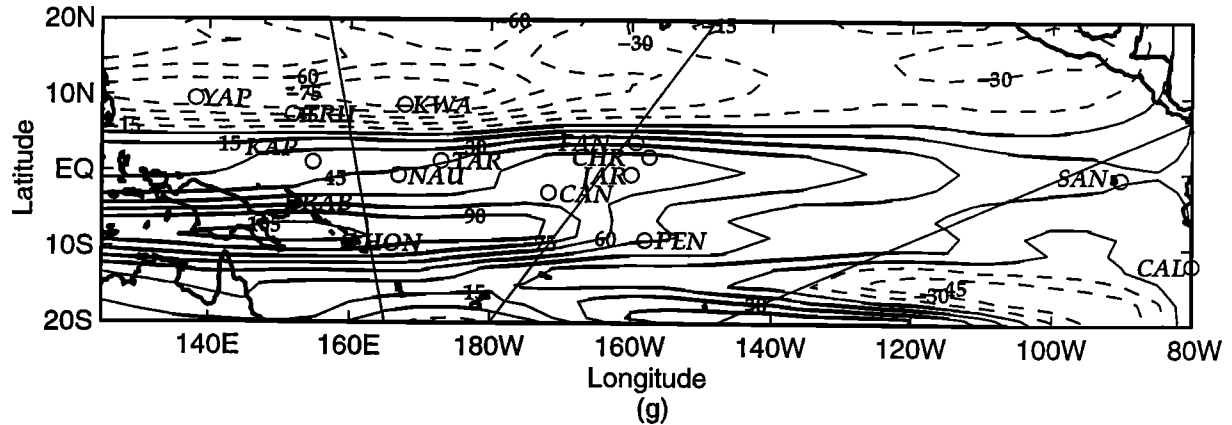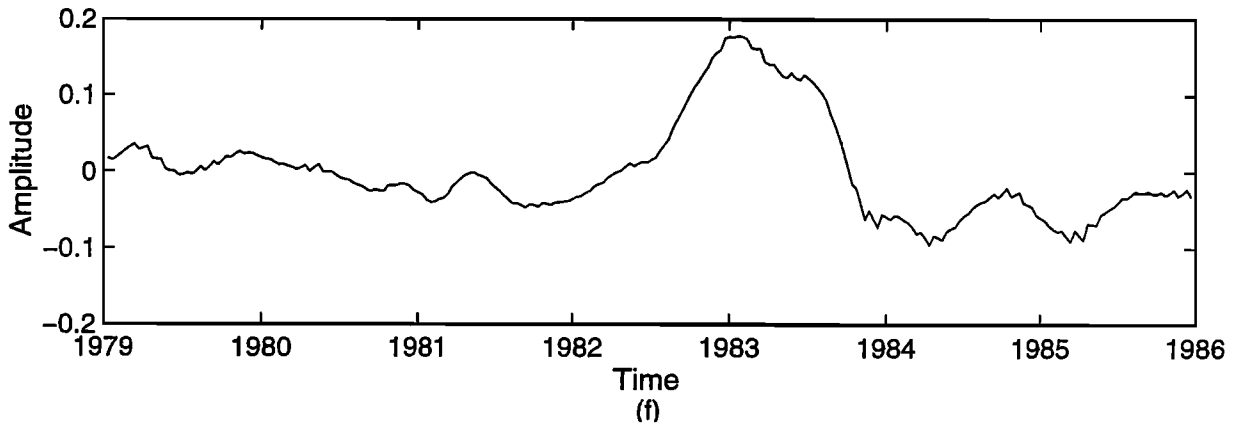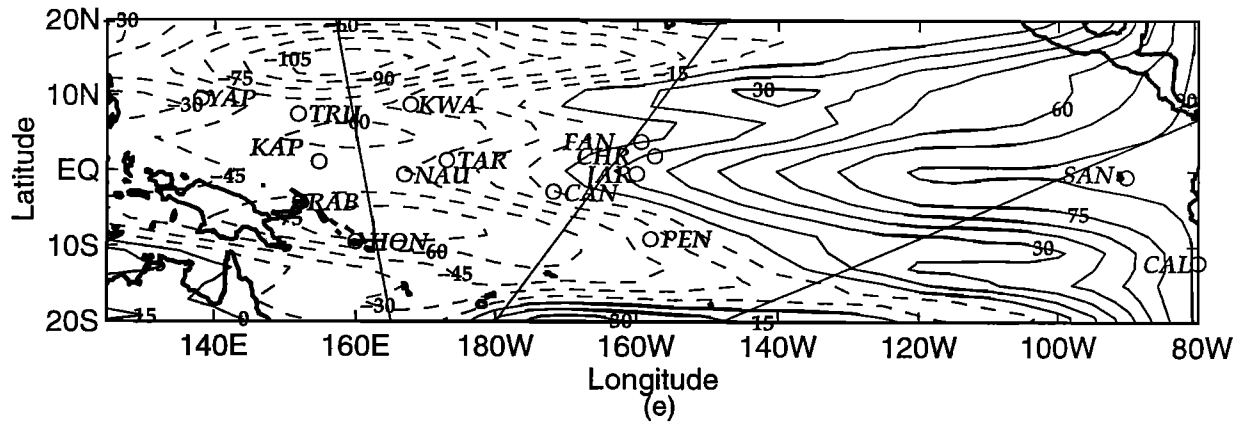
(e)



(f)
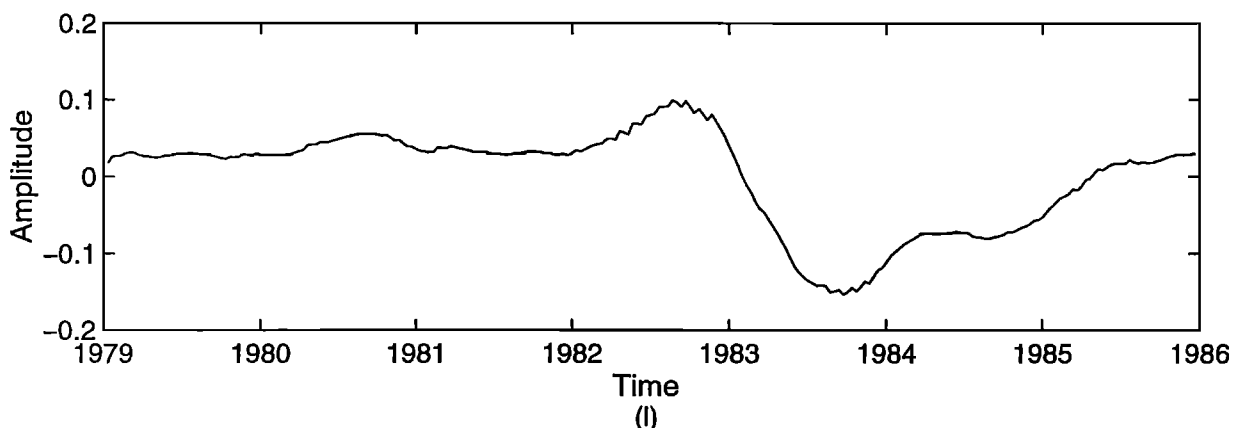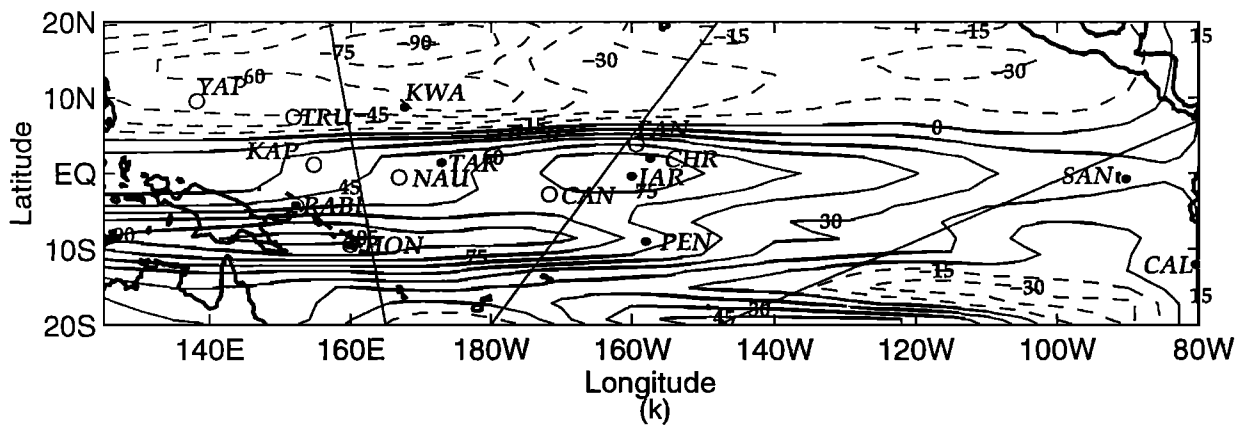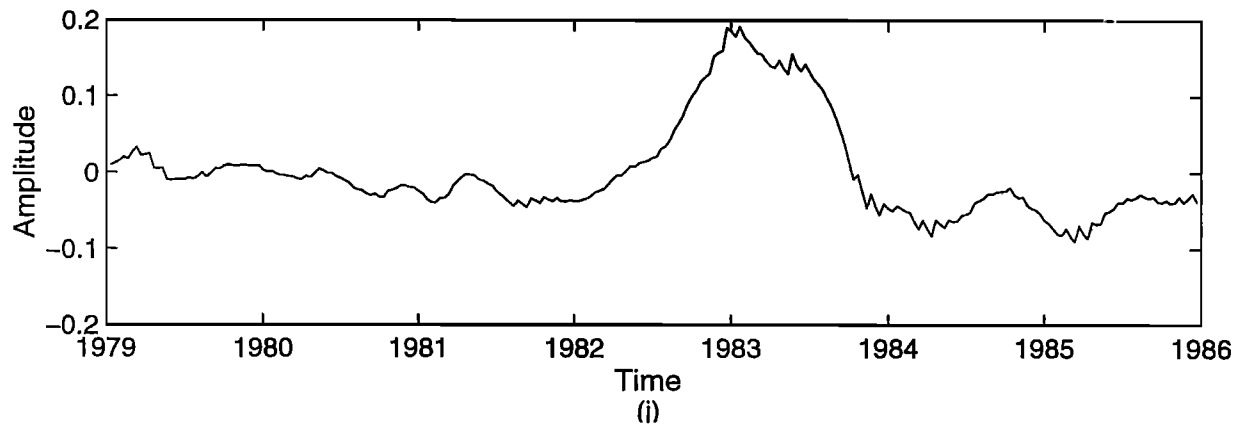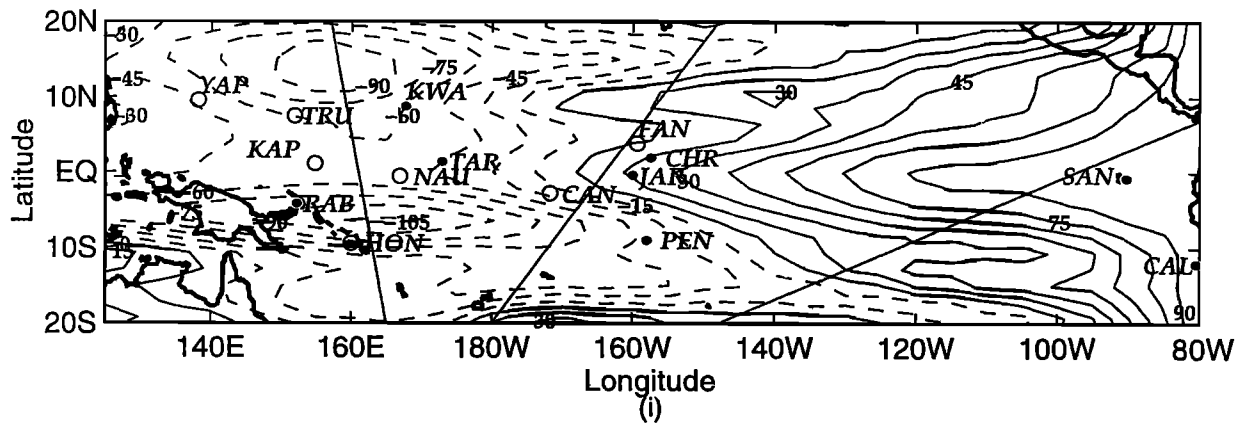


(g)



(h)

**Figure 13.** (continued)

Figure 13. (continued)

**Table 2.** Variances of Time Series of Differences Between Observations and Filter Output, Along With Estimates of These Quantities Generated by the Kalman Filter

| | NODA | | ISL | | XBT | | ISL + XBT | |
|---|---|---|---|---|---|---|---|---|
| | Error Variance | Esti-mate | Error Variance[a] | Esti-mate[a] | Error Variance | Esti-mate[a] | Error Variance | Esti-mate[a] |
| *Sea Level Height Anomaly* | | | | | | | | |
| Station | | | | | | | | |
| Rabaul | 15.9 | 41.4 | (0.8) | (2.5) | 12.9 | 27.9 | (1.5) | (3.3) |
| Nauru | 56.8 | 26.5 | 30.6 | 17.5 | 37.9 | 18.7 | 30.4 | 14.7 |
| Jarvis | 20.0 | 30.8 | (2.4) | (0.4) | 14.0 | 18.9 | (3.6) | (3.2) |
| Christmas | 38.4 | 30.6 | (5.8) | (3.1) | 24.9 | 20.1 | (6.6) | (4.3) |
| Santa Cruz | 41.5 | 31.1 | (3.7) | (4.4) | 25.7 | 16.7 | (8.0) | (5.7) |
| Callao | 32.8 | 42.0 | (1.8) | (3.2) | 16.5 | 24.8 | (1.9) | (3.8) |
| Kapingamarangi | 26.5 | 29.2 | 13.2 | 19.8 | 10.9 | 20.1 | 10.7 | 16.6 |
| Tarawa | 30.1 | 28.3 | (3.0) | (3.5) | 17.6 | 22.6 | (3.2) | (3.9) |
| Canton | 33.1 | 32.2 | 16.0 | 25.7 | 8.4 | 21.3 | 8.9 | 19.7 |
| Fanning | 59.2 | 37.9 | 28.2 | 23.1 | 39.3 | 23.9 | 24.0 | 19.0 |
| Truk | 40.6 | 41.2 | 29.1 | 26.4 | 26.6 | 29.9 | 21.7 | 23.8 |
| Kwajalein | 34.9 | 38.9 | (1.6) | (2.6) | 31.8 | 32.2 | (2.3) | (2.8) |
| Yap | 51.5 | 35.7 | 39.4 | 26.3 | 39.2 | 29.0 | 38.7 | 25.1 |
| Honiara | 51.8 | 36.9 | 41.3 | 28.4 | 42.1 | 22.7 | 48.0 | 20.7 |
| Penrhyn | 34.4 | 37.8 | (2.0) | (2.8) | 36.0 | 32.6 | (2.6) | (3.0) |
| *EOFs of Dynamic Height* | | | | | | | | |
| Track, EOF[b] | | | | | | | | |
| West, 1 | 349.6 | 226.7 | 135.2 | 158.8 | 58.4 | 14.9 | 55.8 | 16.2 |
| West, 2 | 358.9 | 141.3 | 351.6 | 103.4 | 234.5 | 15.5 | 244.1 | 17.9 |
| West, 3 | 181.7 | 155.9 | 141.0 | 116.4 | 53.7 | 11.4 | 57.8 | 12.1 |
| West, 4 | 85.1 | 101.8 | 85.0 | 89.5 | 12.7 | 8.3 | 12.0 | 8.7 |
| Central, 1 | 279.9 | 202.4 | 127.6 | 143.6 | 22.0 | 11.6 | 15.9 | 13.2 |
| Central, 2 | 214.7 | 194.8 | 151.0 | 125.2 | 16.9 | 7.7 | 19.6 | 10.0 |
| Central, 3 | 183.0 | 115.5 | 174.8 | 106.0 | 75.4 | 10.7 | 73.8 | 10.9 |
| Central, 4 | 100.6 | 99.6 | 109.3 | 92.1 | 38.8 | 7.1 | 39.3 | 7.3 |
| East, 1 | 285.8 | 238.4 | 193.3 | 109.1 | 12.4 | 17.1 | 34.7 | 25.9 |
| East, 2 | 108.4 | 111.1 | 98.1 | 102.0 | 19.5 | 28.5 | 19.2 | 29.2 |
| East, 3 | 27.3 | 87.5 | 23.1 | 79.6 | 3.8 | 14.4 | 4.5 | 14.9 |
| East, 4 | 56.0 | 79.2 | 56.6 | 64.4 | 4.2 | 7.8 | 5.8 | 8.6 |

curious since the dynamic height error estimates on the central XBT track at the equator and at 5°N are much closer to the observed variances of the forecast-observed time series. Error estimates at Christmas, Tarawa, Truk, Kwajalein, and Penrhyn are consistently reliable.

One important test of a data assimilation system is the comparison of output of that system with data which do not participate in the assimilation process. There were data from seven such tide gauge stations which were withheld from the assimilation process in all three experiments. Model estimates of the sea level height anomaly at those stations for all three experiments are plotted along with the observations in Figure 14.

Of the examples shown in Figure 14, assimilation seems least effective at Nauru (Figure 14a). Table 2 shows that the RMS errors are reduced by nearly 50%, but the model's weak response during ENSO is not much improved by assimilation. The ENSO response at Truk (Figure 14e), Yap (Figure 14f), and Honiara (Figure 14g) is greatly enhanced by assimilation. At Honiara, assimilation of XBT data appears to be a bit more effective than tide gauge data alone in producing

a faithful representation of the ENSO signal because of the proximity of the western XBT line to the island. Error statistics shown in Table 2 do not reflect this for the entire record at Honiara, but the error estimates are reliable for the nearby XBT record at 10°S on the western track. Improvement is also considerable at Yap and Truk, though the estimates of the error variances are not so good at Yap. The main effect at Kapinga-marangi (Figure 14b), where the error estimates are pessimistic, is in the post-ENSO period from mid-1983 through most of 1984. This is also apparent to a lesser degree in the records at Canton (Figure 14c) and Fanning (Figure 14d).

The assimilation results at the near-equatorial stations Kapingamarangi, Nauru, Canton, and Fanning exhibit strong oscillations. These oscillations are most pronounced at Fanning, where the peak-to-peak amplitude exceeds 5 cm over an assimilation cycle during the ENSO event. This is consistent with the explanation suggested by *Moore and Anderson* [1989] for similar oscillations in their assimilation experiment, which was performed with a similar, if simpler assimilation system. Assimilation of data results in the creation of a pressure

**Table 2.** (continued)

| | NODA | | ISL | | XBT | | ISL + XBT | |
|---|---|---|---|---|---|---|---|---|
| | Error Variance | Esti-mate | Error Variance[a] | Esti-mate[a] | Error Variance | Esti-mate[a] | Error Variance | Esti-mate[a] |
| | | | *Dynamic Height Anomalies* | | | | | |
| Track[c] | | | | | | | | |
| West, -20 | 12.3 | 53.6 | 12.9 | 48.5 | 11.5 | 35.9 | 11.3 | 34.7 |
| West, -15 | 17.1 | 21.1 | 17.5 | 20.3 | 12.3 | 16.9 | 13.4 | 16.3 |
| West, -10 | 31.5 | 29.1 | 25.2 | 25.5 | 14.4 | 18.4 | 17.9 | 17.5 |
| West, -5 | 53.1 | 38.7 | 37.9 | 26.6 | 17.4 | 15.8 | 17.5 | 14.4 |
| West, 0 | 28.6 | 28.9 | 14.3 | 21.7 | 16.3 | 13.5 | 14.9 | 12.6 |
| West, 5 | 31.1 | 43.4 | 31.0 | 36.6 | 21.1 | 25.5 | 21.4 | 24.4 |
| West, 10 | 31.7 | 40.5 | 8.8 | 28.2 | 16.4 | 28.7 | 9.2 | 23.8 |
| West, 15 | 24.0 | 25.1 | 29.1 | 23.9 | 19.3 | 20.9 | 21.3 | 19.6 |
| West, 20 | 53.8 | 21.0 | 55.3 | 20.6 | 62.2 | 18.9 | 58.1 | 18.6 |
| Central, -20 | 24.7 | 59.5 | 25.8 | 51.6 | 25.8 | 34.6 | 25.7 | 33.1 |
| Central, -15 | 21.0 | 23.9 | 16.3 | 22.8 | 12.4 | 19.3 | 10.7 | 18.8 |
| Central, -10 | 51.4 | 33.9 | 40.8 | 23.9 | 18.6 | 21.1 | 23.6 | 18.8 |
| Central, -5 | 46.5 | 42.5 | 39.5 | 37.4 | 21.4 | 22.6 | 22.4 | 21.5 |
| Central, 0 | 15.5 | 36.2 | 11.5 | 25.3 | 12.0 | 14.3 | 11.3 | 13.4 |
| Central, 5 | 42.4 | 34.7 | 35.2 | 27.2 | 23.1 | 17.3 | 19.3 | 16.5 |
| Central, 10 | 23.8 | 25.5 | 21.3 | 24.8 | 15.2 | 20.4 | 13.6 | 20.0 |
| Central, 15 | 12.6 | 16.8 | 13.1 | 16.5 | 11.5 | 13.8 | 10.5 | 13.7 |
| Central, 20 | 48.9 | 15.4 | 50.6 | 14.9 | 50.4 | 13.7 | 50.3 | 13.6 |
| East, -20 | 15.3 | 24.7 | 15.3 | 24.0 | 13.1 | 21.9 | 12.6 | 21.8 |
| East, -15 | 15.7 | 40.8 | 16.8 | 37.7 | 11.1 | 25.5 | 11.2 | 24.9 |
| East, -10 | 11.5 | 28.5 | 9.9 | 27.6 | 6.9 | 20.3 | 7.0 | 20.1 |
| East, -5 | 18.9 | 22.0 | 17.3 | 19.1 | 10.2 | 14.7 | 11.2 | 14.4 |
| East, 0 | 31.1 | 42.3 | 19.8 | 25.4 | 14.3 | 17.8 | 16.0 | 16.4 |
| East, 5 | 31.4 | 44.9 | 21.5 | 31.0 | 5.6 | 21.8 | 8.1 | 21.0 |
| East, 6 | 35.5 | 37.9 | 23.9 | 20.8 | 10.5 | 16.5 | 11.8 | 14.6 |
| East, 7 | 47.0 | 63.9 | 33.2 | 31.4 | 20.8 | 31.8 | 21.7 | 24.0 |

Statistics are given for time series of sea level height anomalies at tide gauge stations, amplitudes of EOFs of XBT-derived dynamic height anomalies, and dynamic height anomalies at selected locations.

NODA is the run without data assimilation. ISL is the run in which data from a selection of tide guages were assimilated. XBT is the run in which the four leading empirical orthogonal functions (EOFs) of the XBT data were assimilated. ISL+XBT is the run in which both tide gauge and SBT data were assimilated.

[a]Numbers in parentheses refer to Stations from which data were assimilated.

[b]Numbers refer to the four EOFs used.

[c]Number are degrees latitude.

gradient which is not balanced by the wind. Between updates, this pressure gradient relaxes by the generation of equatorially trapped waves. These oscillations are stronger at Canton and Fanning than at Kapinga-marangi and Nauru. This is consistent with Moore and Anderson's general finding that this phenomenon was more pronounced in the eastern half of the basin.

Sea level height anomaly is contoured on the $x$-$t$ plane along the equator in Plate 1 for the experiment with no data, all three assimilation experiments, and for the objective map of the data. *Moore and Anderson* [1989] presented their results on a single-layer reduced gravity model driven by the FSU wind stress data set, with XBT data assimilated along sections similar to those we consider here. Direct comparison of their results to ours is difficult, but the variation in their experiments is comparable in magnitude to ours.

The lack of temporal smoothness in the output of the filter is readily apparent in these $x$-$t$ plots. Note also the prominence of the ENSO event and the changes

from one run to the next. From the center of the basin eastward, sea level anomalies associated with the 1982-1983 ENSO event appear in the assimilation runs, with amplitudes nearly double those of the runs without assimilation. Later on in the simulation, the positive anomalies which appear in the western part of the basin beginning in late 1983 in the run without assimilation do not appear in the assimilation runs until mid-1984, and then they are weaker and more confined near the western boundary, as in the objective maps of the observations. Fairly strong negative anomalies appear in the eastern half of the basin in 1985. They are strongest in the simulation with no assimilation. All of the assimilation runs appear more like the data (Plate 1e) near the eastern boundary during this period, as would be expected. The maps from the ISL and ISL+XBT experiments extend these anomalies westward, nearly to 140°W.

Maps of estimated RMS sea level error are shown in Figure 15. These should be compared with that shown

in Figure 7b of the model without assimilation. In Figures 15a–15c the characteristic pattern appears. Errors are fairly homogeneous in the zonal direction near the equator, with strong meridional gradients at about 4°N and 4°S, west of about 160°W. A characteristic pattern also appears east of about 110°W in Figures 15a–15c and in Figure 7b. Assimilation in all three experiments results in accuracy near the 3-cm RMS instrument error over most of the basin between 4°N and 4°S, with a wider meridional range east of 110°W.

Figure 15a shows the effect of updating at the island tide gauge stations alone. Near the equator, the pattern is similar to the one obtained without updating (Figure 7b), but the errors are quite a bit smaller. Updating at the off-equatorial stations at Kwajalein and Penrhyn has an effect that is limited in the meridional direction

but extends tens of degrees westward, indicating propagation of information by Rossby waves.

Figure 15b shows the effect of assimilating the EOF amplitudes of the dynamic heights. The appearance of the typical pattern indicates the introduction of Kelvin and low meridional mode Rossby waves into the analysis through the XBT information. Along the eastern track the assimilation has little effect west of the track itself. *Sheinbaum and Anderson* [1990] found assimilation of XBT data in the eastern part of the basin similarly ineffective in influencing the analysis in the western portion of the domain. Information from the western track does, however, seem to propagate westward. This effect is more pronounced south of the equator, where the central and western tracks converge. Careful examination of this map along the western track shows the character-
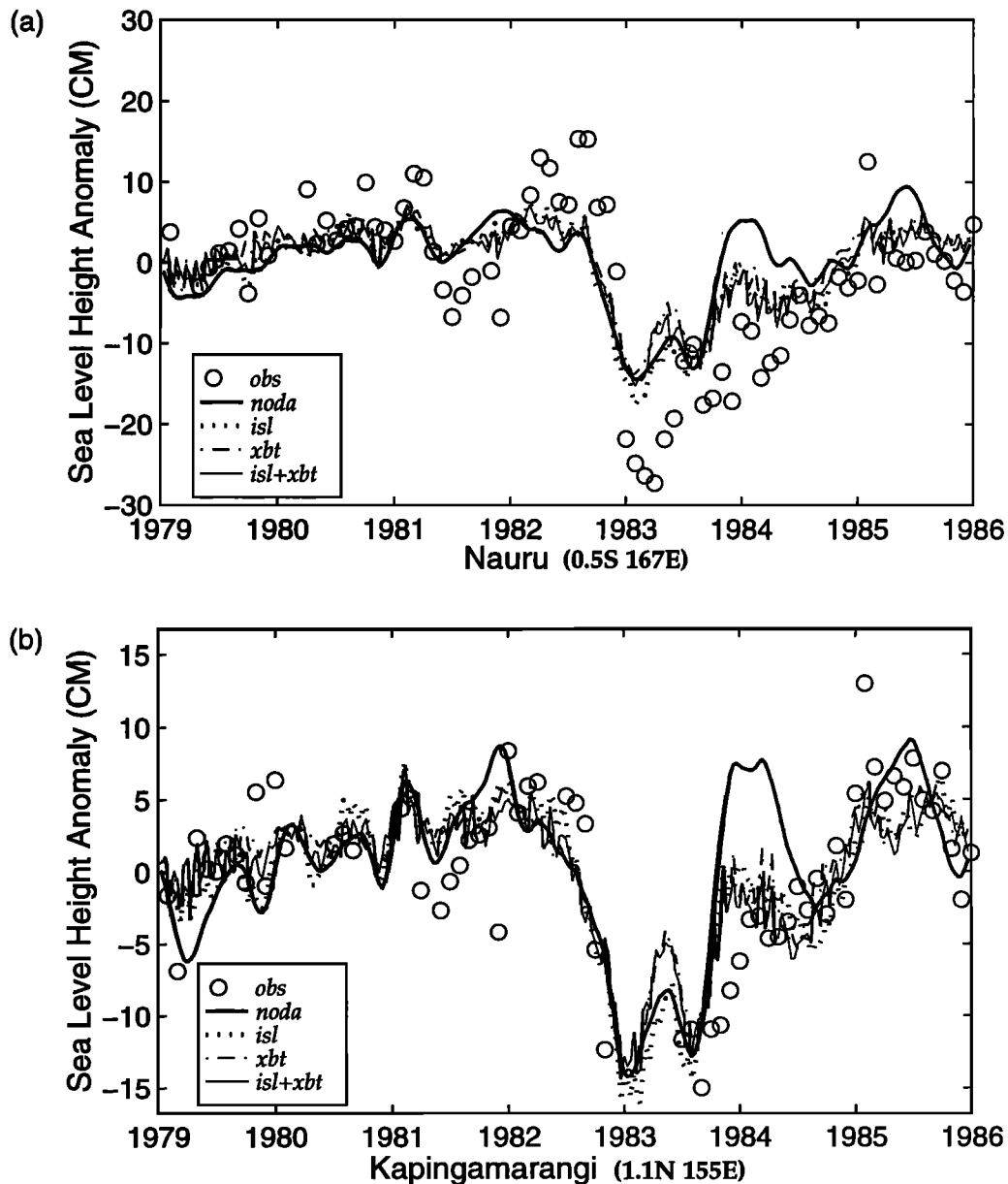


**Figure 14.** Time series of sea level height anomaly at withheld tide gauge stations (a) Nauru, (b) Kapingamarangi, (c) Canton, (d) Fanning, (e) Truk, (f) Yap, and (g) Honiara.
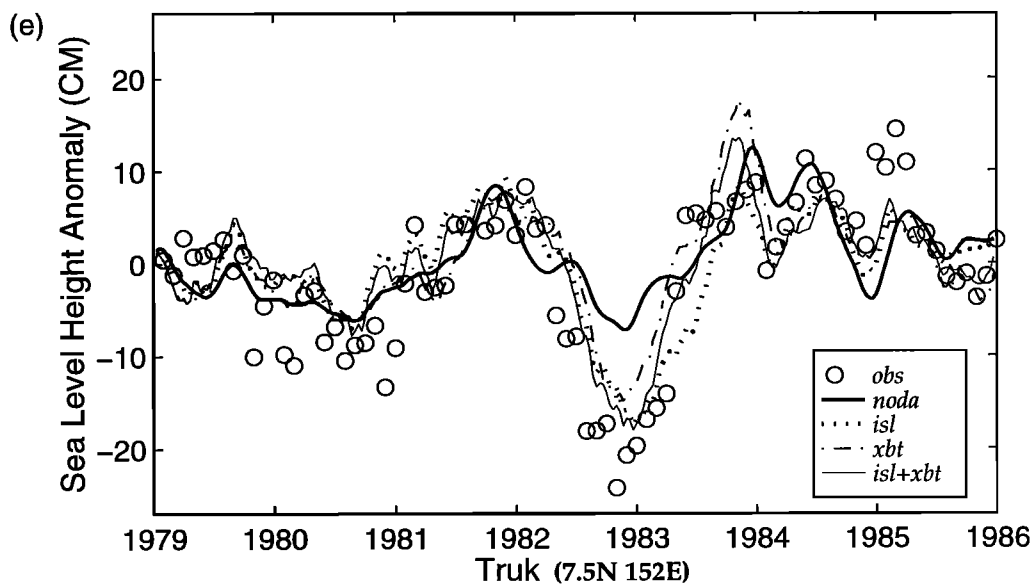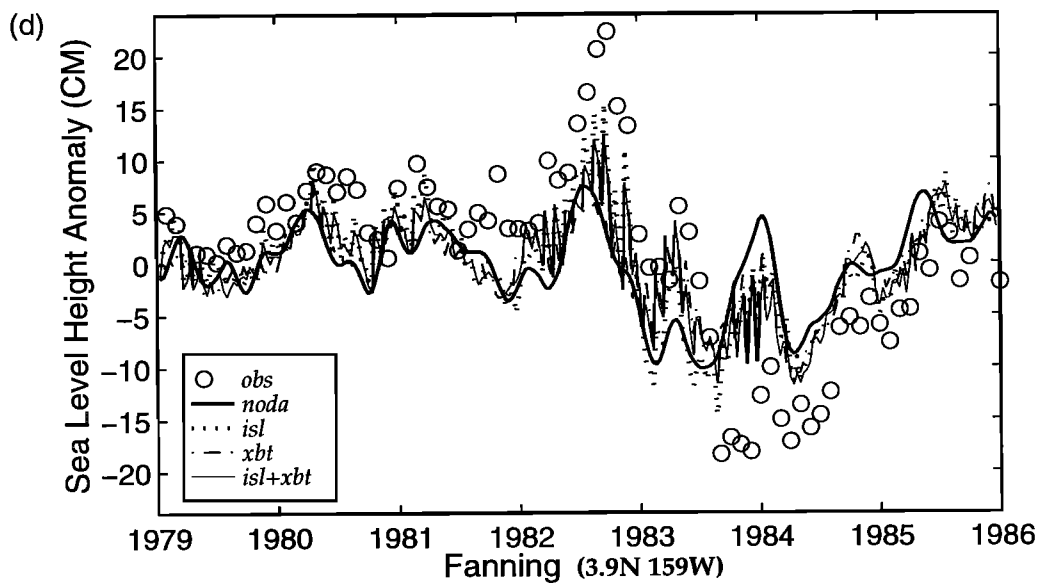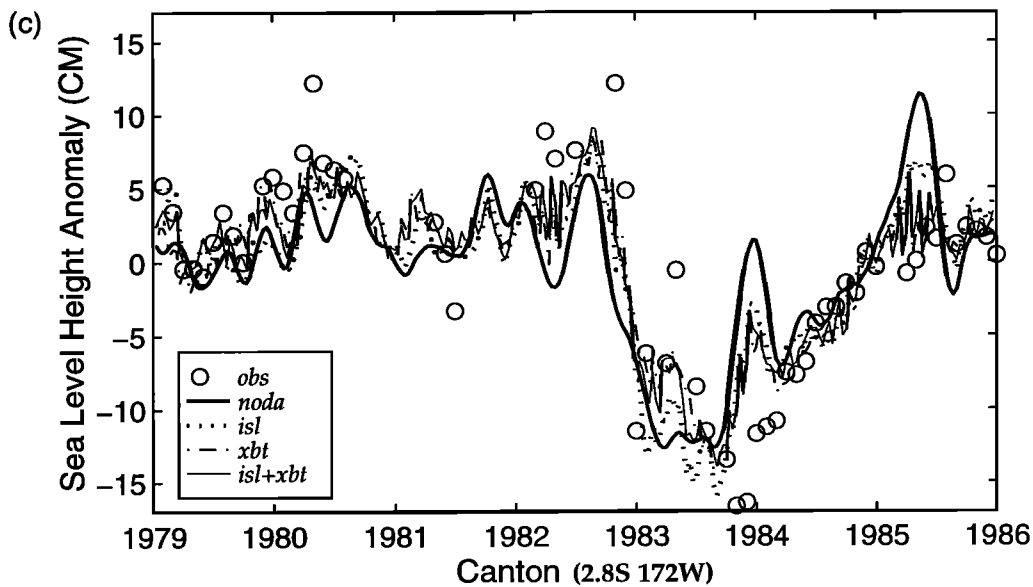
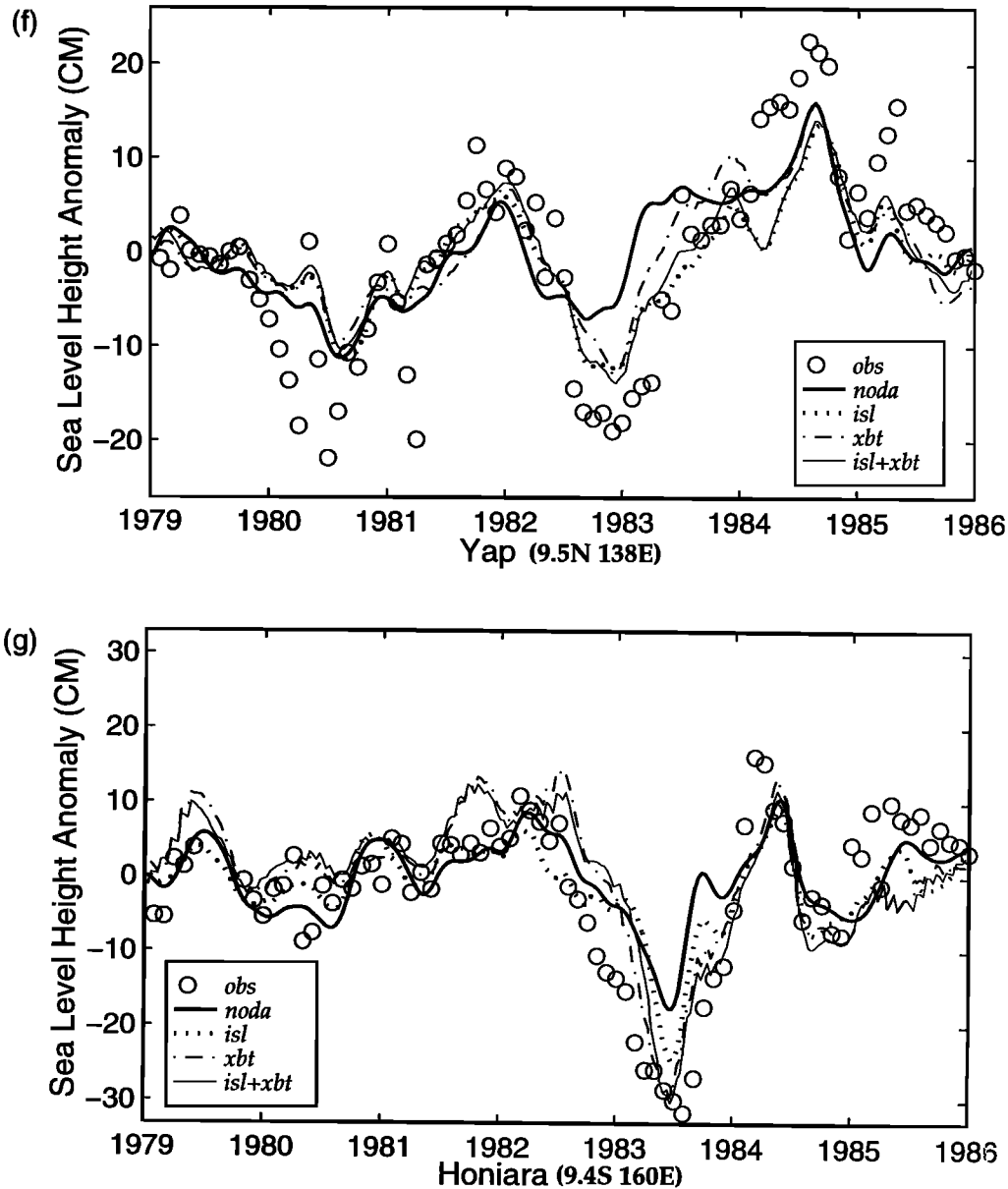**Figure 14.** (continued)

**Figure 14.** (continued)

istic strong meridional gradient near 4°N nearly intact, while the corresponding structure near 4°S is considerably weakened, with enhanced accuracy extending west of Honiara.

Figure 15c shows the combined effect of assimilating XBT sections and tide gauge stations. It shows a region of enhanced accuracy near 150°E, 10°S, owing, evidently, to the combined effects of assimilation of data at Rabaul and along the western XBT track. Assimilation of data along the central track seems to complement the effect of data at Penrhyn, producing a region of enhanced accuracy that extends west from Penrhyn almost to the western boundary. In the northwest and in the east, as expected, the result of assimilating the two data types retains the enhanced accuracy of both of them.

These effects are shown clearly in Figure 16, in which differences between the estimated error variance maps from the assimilation runs and the run without assimilation are shown. In Figure 16a the shape of the influence of the data at Rabaul, Kwajalein, and Penrhyn is clearly apparent. We also have yet another view of the relative lack of influence of stations in the eastern part of the basin on the analysis much to the west of the data sites.

Examination of Figures 16a and 16c and comparison of them with Figure 16b show that the major effect of assimilation of data at Santa Cruz and Callao is to establish the general pattern near the eastern boundary. Influence of data from these two stations is trapped near the boundary for the most part, spreading westward no farther than 100°W along the equator. It is also clear
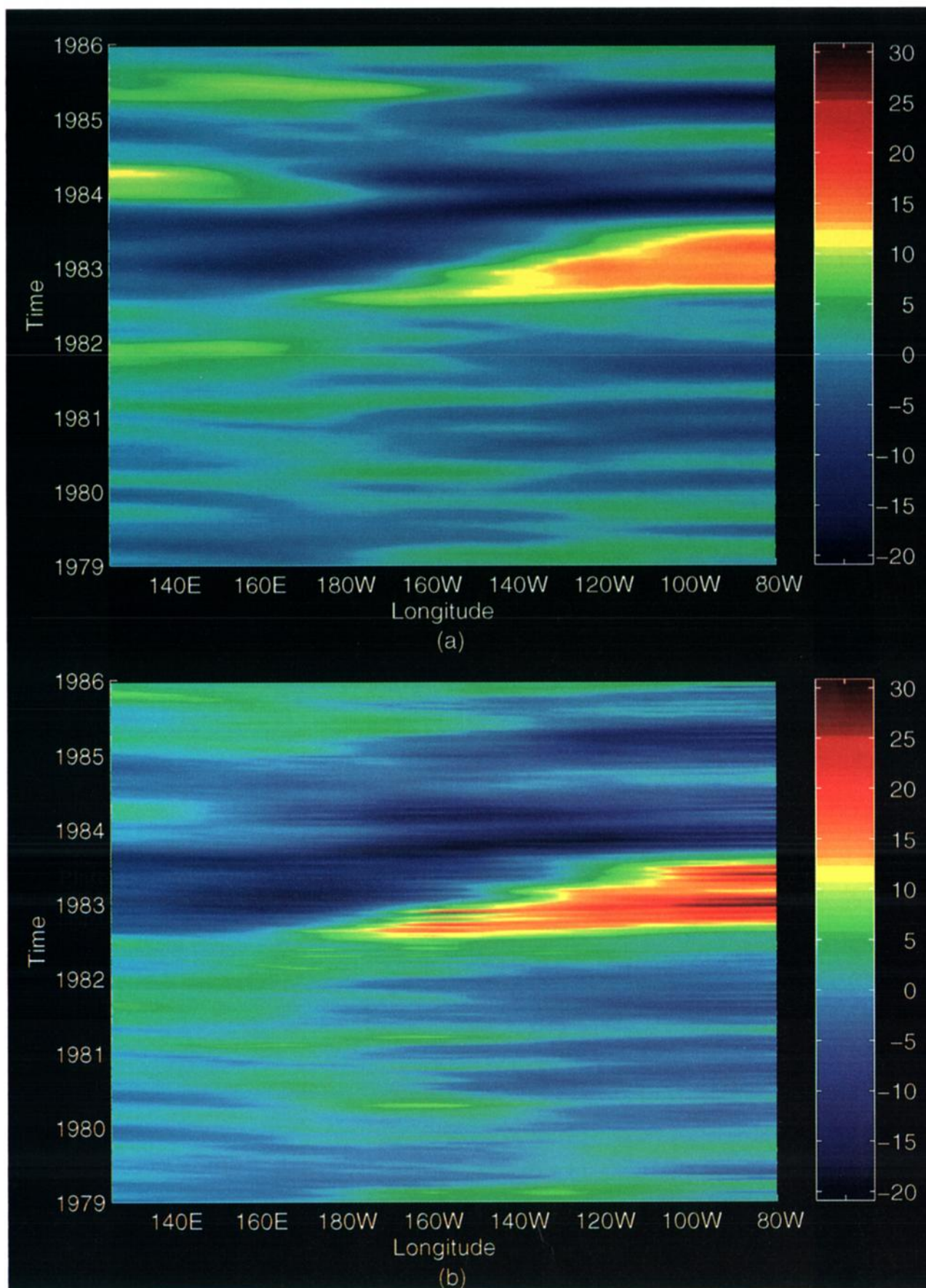
**Plate 1.** *x-t* plots along the equator for all experiments and for objective analysis of the data without reference to the model for (a) NODA, (b) ISL, (c) XBT, (d) ISL+XBT, and (e) objective map of data alone.
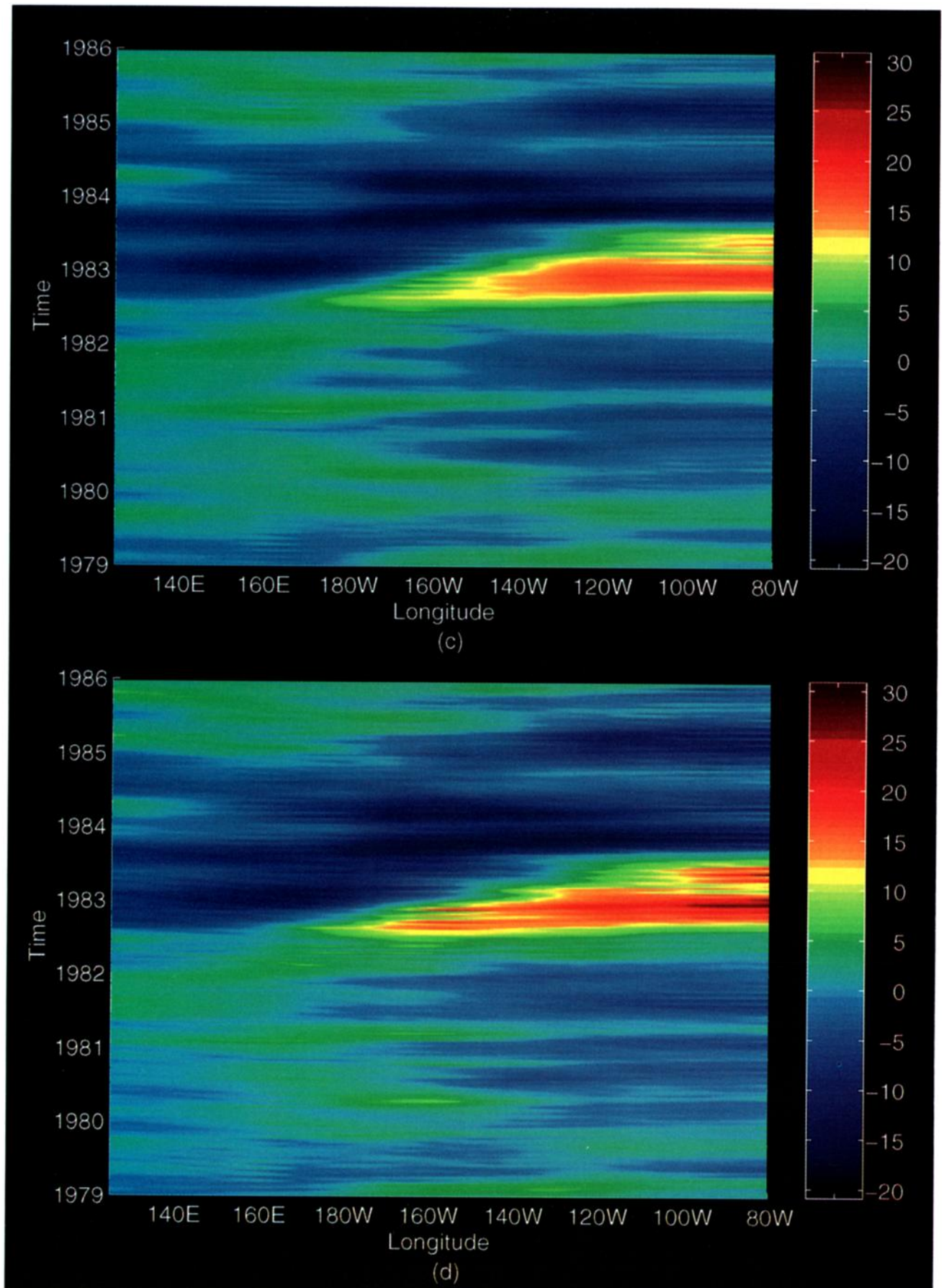
(c)



(d)

**Plate 1.** (continued)

that the assimilation process does not fill the data void from about 120°W to 150°W along the equator. This emphasizes the importance of the TOGA-TAO lines in this region, which were not present during this time period.

Figure 16b shows that the impact of the central and western XBT tracks is widespread but fairly weak. The difference in the estimated RMS errors between XBT and NODA is rarely more than 1.5 cm, but the range of this influence spreads westward from the central track to the western boundary in a band of latitudes from 10°S to 10°N. When the island tide gauge stations are added, the total influence is extended eastward from the central track, owing to the addition of assimilation stations at Penrhyn, Jarvis, and Christmas. Just east of the central track, Figure 16c resembles Figure 16a. The combined effect of the XBT and island station data is most evident west of the western track, where the combination of data from the western XBT track and the tide gauge station at Rabaul gives rise to enhanced accuracy south of the equator from 160°E nearly to the western boundary.

Figure 16b shows another view of the difference in effectiveness of assimilation of data from the eastern and western tracks. In particular, the meridional asymmetry of the influence of the western track is apparent.

The relatively poor quality of the error estimate at Yap might be ascribed to its poleward position near the western boundary. At that location it may be affected by the artificial meridional boundary at 125°E. It is also worth noting that the differences between this model and the more detailed model of *Gent and Cane* [1989] occur in the northwestern and southwestern parts of the model domain.

It would be desirable to know how much the variances of the residual (i.e., model minus observed) time series change from one realization to another. The strong serial correlation in those time series casts severe doubt on the use of the bootstrap to estimate this quantity, so we cannot assign confidence intervals to the hypothesis that the difference between our error estimates and the residual time series can be explained in terms of differences between samples drawn from the same underlying population.

## 6. Discussion and Summary

The clearest effect of data assimilation in this system is to restore the signal amplitude to the analysis which is lacking in NODA, the model run without assimilation. From this consideration alone the analysis resulting from the assimilation scheme should be considered a
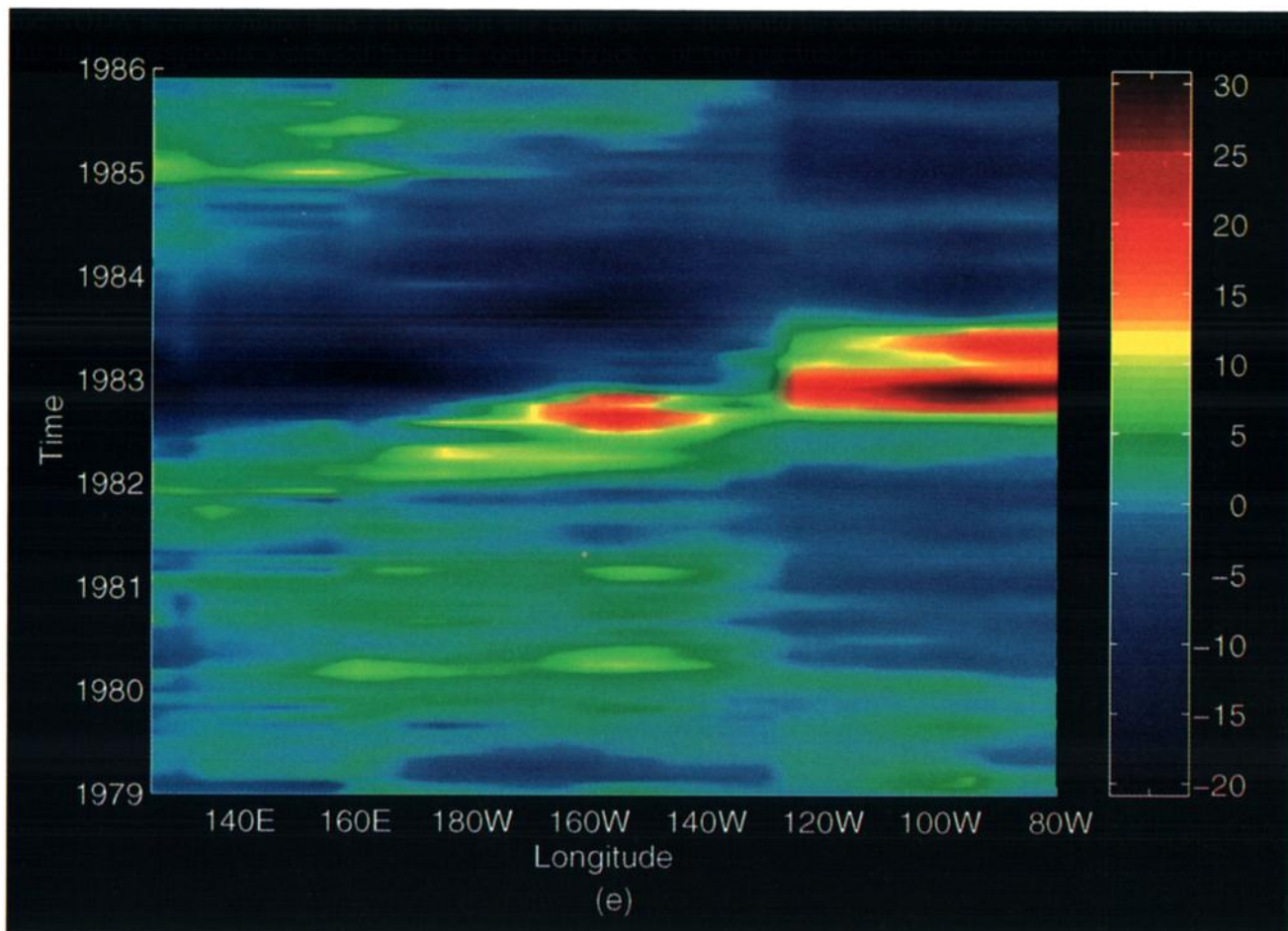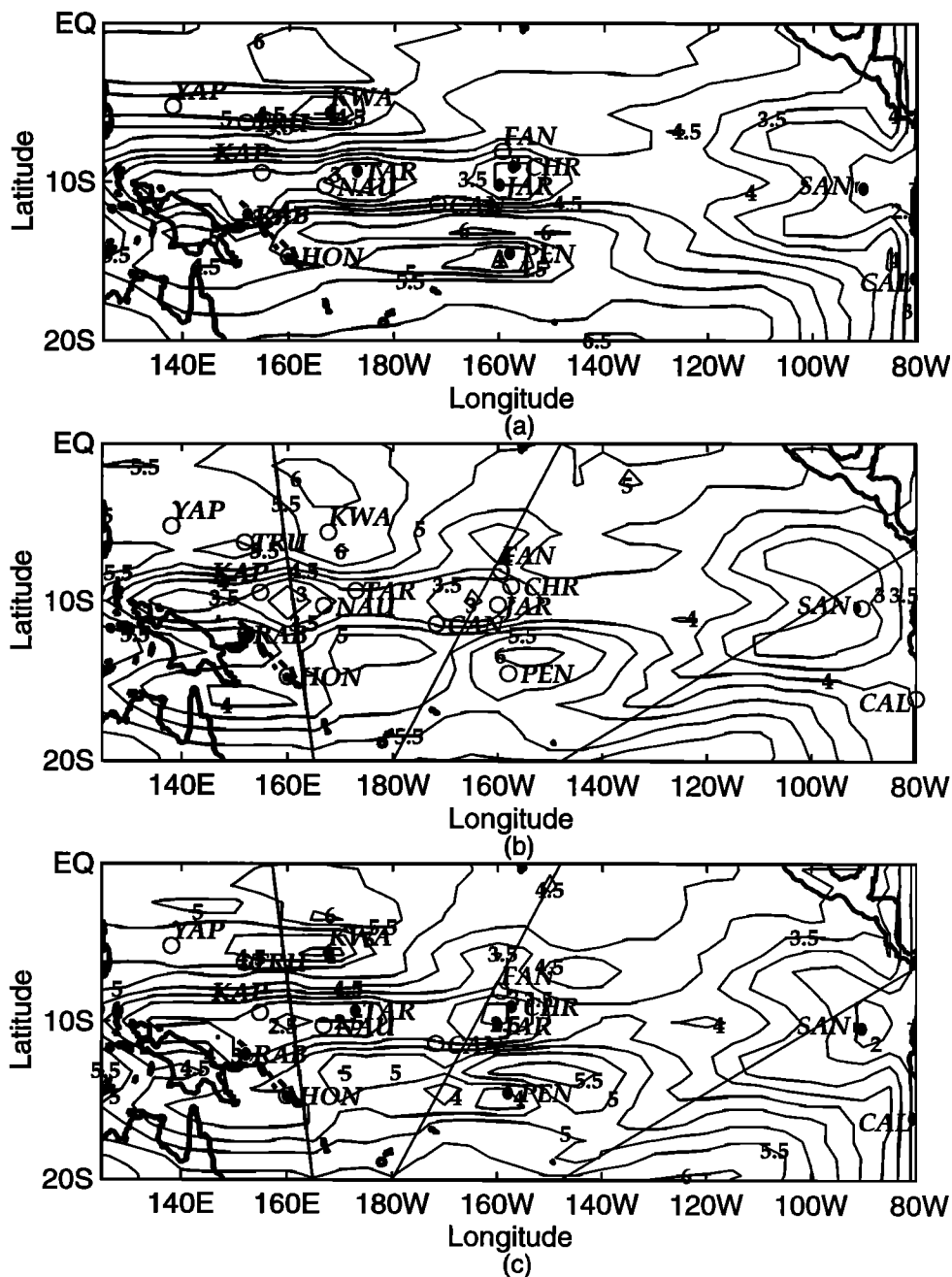


Plate 1. (continued)

**Figure 15.** Model-generated estimates of RMS sea level height errors for each of the three assimilation runs, (a) ISL, (b) XBT, and (c) ISL+XBT.

more faithful representation of the true large-scale, slow timescale variation of dynamic topography of the tropical Pacific than either the model output, which is too weak, or the statistical objective analysis of the data, which, reflecting the sparseness of the data and lack of dynamics, is no stronger than NODA in data-void regions.

Practical benefits of these improvements from the data assimilation remain uncertain at this point. However, coupled atmosphere-ocean studies of the ENSO phenomenon suggest that the lead time in ENSO predictions may be due to the inertia of the subsurface

thermal field in the tropical Pacific Ocean. If so, one might expect that it would be important to initialize coupled prediction models with the correct amplitude of the deviations in the subsurface thermal structure or the vertical integral thereof, i.e., dynamic topography. For example, if off-equatorial wave processes are important to the evolution of the ENSO cycle, then the amplitude improvements seen at the off-equatorial locations of Figures 14e, 14f, and 14g in late 1982 and early 1983 may be significant in initializing westward propagating upwelling Rossby waves and the subsequent termination of the warm phase of ENSO.
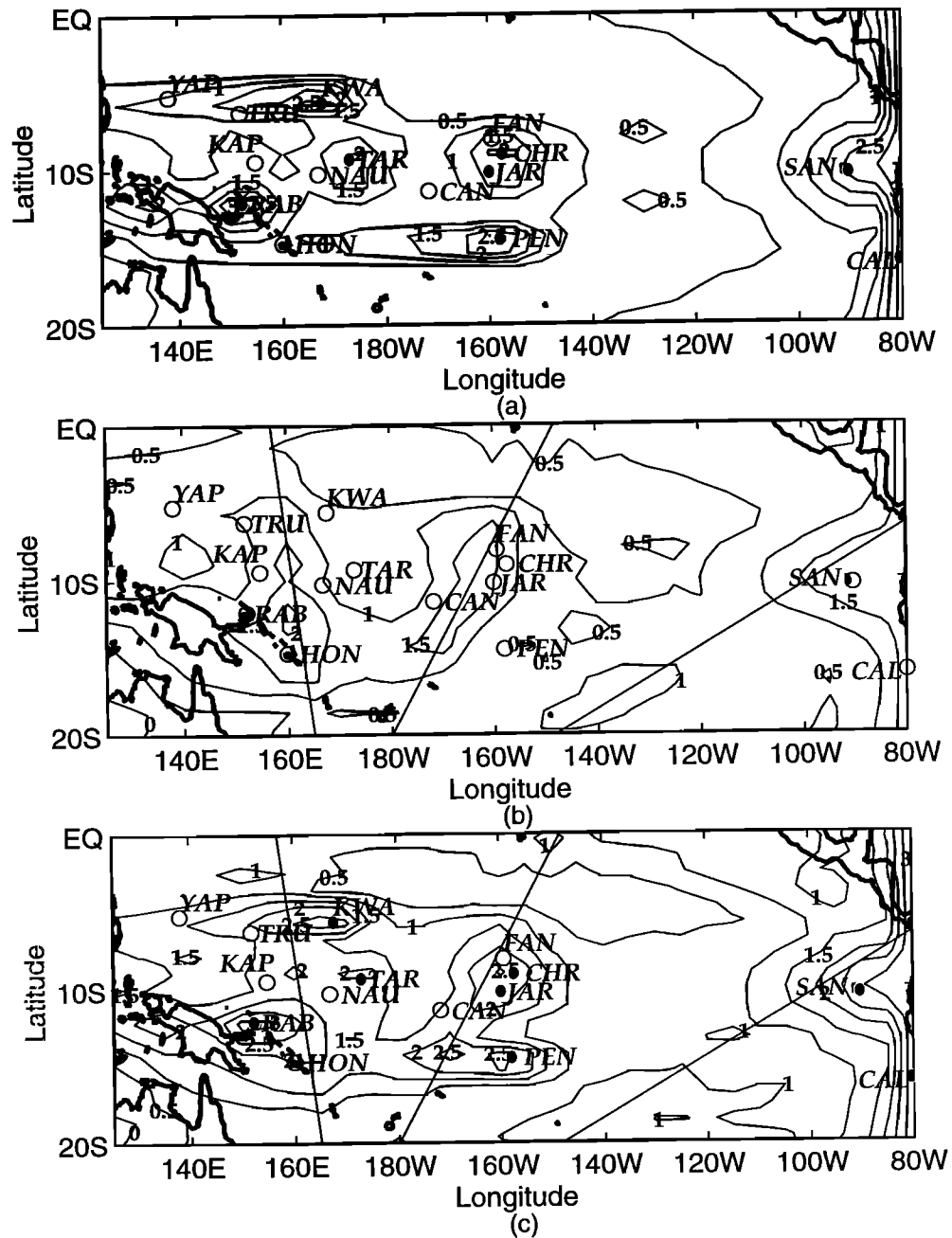
**Figure 16.** Difference between model-generated estimates of RMS errors for assimilation runs and the run in which no data were assimilated, i.e., the difference fields between Figure 15 and Figure 7. (a) ISL minus NODA, (b) XBT minus NODA, and (c) ISL+XBT minus NODA.

The basis of any data assimilation scheme lies in the error models, which determine the weights to be placed on model output and observations. Impact of any observation on the analysis necessarily depends on the estimates of the errors in the model. Practical error models must be determined by a manageable number of parameters. Of the parameters in our Kalman filter, the meridional decorrelation length of the system noise has the greatest effect on the analysis. This quantity is related to the error in the wind stress curl. If it is set too small, the result will be a drastic overestimate of the error in the sea level outside of a narrow band of latitudes near the equator.

One obvious weakness of most error models associated with published data assimilation schemes is the assumption of statistical homogeneity of the system noise. We constructed an inhomogeneous noise model based on the difference field between two wind products but did not find great improvement over the simple homogeneous one.

Various other schemes for estimating inhomogeneous error covariance fields were considered. One could, for

example, assume that the homogeneous $\mathbf{Q}$ is a first guess and then use the formula from the Kalman filter for calculating the forecast error covariance to calculate an "updated" $\mathbf{Q}$, based on the assumption that the error field is updated where the observations are most dense. Given the large range of error variances, it would be difficult to distinguish between the results of experiments with different parameter values.

There is every reason to expect the zonal and meridional model error decorrelation lengths $L_x$ and $L_y$ (see (7)) to be nonconstant functions of space. We therefore attempted to estimate spatial variations of these quantities directly from differences between the FSU wind product and the SSM/I product. We expect these statistics to reflect the inhomogeneity of the errors in the FSU wind field because of the relative uniformity of the SSM/I data coverage. The errors in the SSM/I winds are not exactly homogeneous because they contain the statistical properties of the analysis used to determine the wind direction. *Busalacchi et al.* [1993] calculated the variance field of the differences between these two products. *Halpern and Wentz* [1994] compared the wind time series for the interval from December 1990 to November 1991 from two simultaneously orbiting SSM/I instruments. They found that the RMS difference of the monthly mean wind speed from the two instruments to be about 1.5 m/s over the tropical ocean, with relatively small temporal variation. This can be taken as a rough estimate of the magnitude of the wind speed errors in the SSM/I data, which are thus comparable to those found in the FSU data set.

We attempted to evaluate the spatial variation of $L_x$ and $L_y$ by performing the following set of calculations: let $e_{ij}(t_k)$ be the difference between the SSM/I and FSU data sets at $x = x_i$, $y = y_j$, and $t = t_k$. We chose a set of fixed coordinates $(x_I, y_J)$ and calculated the sample correlations $R(x_I, y_J, x_i, y_j)$ of the difference fields relative to $(x_I, y_J)$ according to the formula

$$
\begin{aligned}
&R(x_I, y_J, x_i, y_j) \\
&= \;[(N-1)/N]\left[\sum_{k=1}^{N} e_{IJ}(t_k) e_{ij}(t_k)\right] \\
&\quad \cdot \left[\left(\sum_{k=1}^{N} e_{IJ}^2(t_k)\right)\left(\sum_{k=1}^{N} e_{ij}^2(t_k)\right)\right]^{-(1/2)}
\end{aligned}
$$

for $(x_i, y_j)$ near $(x_I, y_J)$. Systematic variation in the maps of $R$ for different points $(x_I, y_J)$ could be taken as evidence of systematic variation of error correlation scales. These calculations did not yield clear evidence of inhomogeneity of spatial correlation scales. This may be due, at least in part, to the small number of degrees of freedom in the data used to calculate the statistics. When the homogeneity assumption is discarded, each correlation value is the result of a small number of samples. It is therefore not surprising that the results were quite noisy, and this noise may have hidden large-scale features of the error field.

Our model of errors in the hydrographic data is certainly oversimplified. *Taft and Kessler* [1991] con-

structed a detailed error model based on comparisons with conductivity-temperature-depth (CTD) data. Their model included a contribution from random instrument errors of 1.69 dyn. cm. They also found that errors due to use of the climatological T-S relation were well correlated over times of several months and therefore could not be assumed to be diminished by repeated sampling, as we assumed. Their model included an explicit calculation of the meridional correlation of dynamic height errors which would be better fitted by an exponential than by a Gaussian. This presents a technical problem since the derivatives of the correlation function at $\Delta y = 0$ are physically meaningful, and therefore smooth functions should be chosen to model them.

For all of the defects in our error model for the hydrographic data, a more sophisticated model such as that of *Taft and Kessler* [1991] would make little difference in an assimilation scheme such as this one. According to the Taft and Kessler model, the dynamic height errors in the western, eastern and central tracks are 11.3, 10.8, and 12.3 cm$^2$, respectively. Use of these numbers instead of the ones we used would have made no discernible difference in Figure 6 and would have changed the figures in the NODA columns of Table 2 by 0.1 cm or less.

We also recalculated the estimated error variances of the EOF amplitudes based on *Taft and Kessler's* [1991] model, with the spatial correlation function for the errors due to use of the mean T-S dependence shown by *Taft and Kessler's* [1991, Figure 13b] fitted roughly by $\exp(-|\Delta y|/4°)\cos(\pi y/10°)$. Other error sources were assumed to be uncorrelated with those in other latitude bins. The resulting figures were slightly smaller than those shown in Table 1. If anything, this would have made the comparisons in Table 2 a bit worse, but the effect would have been small in any case.

In an attempt to determine the extent to which we have realized the optimal filter, we examined the innovation sequences. These are the vectors multiplied in (3) by the Kalman gain $\mathbf{K}_{k+1}$ to form the correction to the forecast.

They take the form $(\mathbf{w}_{k+1}^o - \mathbf{H}_{k+1}\mathbf{w}_{k+1}^f)$. It was first shown by *Kailath* [1968] that in an optimal linear filtering system the innovation sequence is not serially correlated. Intuitively, if the filter is extracting all possible information from the data, then the innovation sequence should be white. Color in the innovation sequence indicates that there is information still to be extracted.

*Daley* [1992b], in a series of experiments on a simplified system, showed how the autocovariance of the innovation sequence can be used as a performance diagnostic in a data assimilation system and applied his results to forecasts for central North America produced by the Canadian Meteorological Centre data assimilation system. In that case, distinctive patterns appeared in the plots of the lagged innovation correlations relative to Omaha, Nebraska. In the present case, the data are too sparse to determine phase relations of the au-

**Table 3.** Autocorrelations of Innovation Sequences

| Island | Autocorrelation | Autocorrelations By Track | | | |
|--------|-----------------|------|------|---------|------|
| | | EOF | West | Central | East |
| Rabaul | 0.63 | 1[a] | 0.87 | 0.90 | 0.74 |
| Jarvis | 0.68 | 2 | 0.83 | 0.89 | 0.67 |
| Christmas | 0.70 | 3 | 0.79 | 0.86 | 0.68 |
| Santa Cruz | 0.73 | 4 | 0.68 | 0.76 | 0.73 |
| Callao | 0.65 | | | | |
| Tarawa | 0.65 | | | | |
| Kwajalein | 0.48 | | | | |
| Penrhyn | 0.20 | | | | |

Correlation statistics were calculated for stations participating in the assimilation. Statistics for island stations are for experiment ISL, in which data from a selection of tide gauges were assimilated. Statistics for EOFs are for experiment XBT, in which the four leading EOFs of the XOT data were assimilated.

[a]EOF 1 is most significant.

tocorrelation statistics, and no clear conclusions can be drawn.

*Dee et al.* [1985] devised a method for determining **Q** and **R** adaptively by minimizing the lagged autocorrelation of the innovation sequence. That method has the advantage of being able to deal with nonstationarity, but is quite cumbersome in application, and would not be practical for a problem of this size.

The autocorrelations of the innovation sequences for assimilation of island tide gauges and of EOFs of XBT dynamic height sections at 1-month lag are shown in Table 3. Lagged autocorrelations at 2-month lags and beyond are quite a bit smaller, for the most part, though some are significantly different from zero. Similar calculations were performed for the experiment in which data from both sources were assimilated, and the results were essentially identical. These results are disappointing, indicating as they do that the filter is operating far from optimally. The only exception is at Penrhyn. Referring to Table 2, the error variance estimates at Penrhyn are among the most reliable in our series of experiments.

Despite the fact that our filter is far from optimal, we believe that only marginal improvement is available within the current framework. In our experiments we have found very little sensitivity to parameters which determine the system and observation noise matrices. Our analysis is probably the best available for this time period, given the assumption that the difference between the model and reality is well described by additive white noise. The vast majority of published data assimilation schemes contain either this assumption or the simpler assumption that the model and forcing data are exact representations of nature.

It may well be possible to achieve better results by dropping the hypotheses that the forecast and observation errors are stationary, white, and uncorrelated with the signal amplitudes. *Taft and Kessler* [1991] calculated the temporal autocorrelation structure of the dynamic height error explicitly and found significant autocorrelation out to several months. Similarly autocorrelated errors have been noted in the tide gauge data also (G. Mitchum, personal communication, 1994). Finally,

the errors are almost certainly nonstationary, owing to the influence of the ENSO cycle. It will be necessary to take these factors into account in the construction of better filters, even for linear models.

*Moore and Anderson* [1989], who used a single-layer reduced gravity model, and *Kawabe* [1994], who used a model similar to the MC model, also found that model sea level response to the FSU winds was too weak during the 1982–1983 ENSO event. It is likely that the forcing contains systematic errors which are not well described by stationary white noise. If there are, e.g., systematic biases in the forcing data, we would expect the innovation sequence to be highly temporally correlated. Even in this case, *Hao and Ghil* [1994] showed in a series of simulation experiments that the CP model with section data similar to our XBT lines assimilated by optimal interpolation would perform well.

In future studies our focus will be directed toward the observations taken during the TOGA decade (1985–1994). In addition to the tide gauge and XBT observations used here, we will also incorporate the thermal field measurements from the TOGA-TAO array and radar altimeter measurements from the Geosat, ERS 1, and TOPEX missions. Of particular interest will be a determination of the value added by the various data types for both the monitoring and prediction of ENSO variability.

# References

Bennett, A. F., Inverse methods for assessing ship-of-opportunity networks and estimating circulation and winds from tropical expendable bathythermograph data. *J. Geophys. Res.*, *95*, 16,111–16,148, 1990.

Bennett, A. F., *Inverse Methods in Physical Oceanography*, 346 pp., Cambridge University Press, New York, 1992.

Bennett, A. F., and W. P. Budgell, The Kalman smoother for a linear quasi-geostrophic model of ocean circulation, *Dyn. Atmos. Oceans*, *13*, 219–267, 1989.

Budgell, W. P., Stochastic filtering of linear shallow water wave processes, *SIAM J. Sci. Stat. Comput.*, *8*, 152–170, 1987.

Busalacchi, A. J., and F. Blanc, On the role of closed and open boundaries in a model of the tropical Atlantic ocean, *J. Phys. Oceanogr.*, *19*, 831–840, 1989.

Busalacchi, A. J., M. J. McPhaden, J. Picaut, and S. R. Springer, Sensitivity of wind-driven tropical Pacific ocean simulations on seasonal and interannual time scales, *J. Mar. Syst.*, *1*, 119–154, 1989.

Busalacchi, A. J., R. M. Atlas, and E. C. Hackert, Comparison of SSM/I vector wind stress with model-derived and subjective products for the tropical Pacific, *J. Geophys. Res.*, *98*, 6961–6977, 1993.

Cane, M. A., and R. J. Patton, A numerical model for low-frequency equatorial dynamics, *J. Phys. Oceanogr.*, *14*, 1853–1863, 1984.

Chelton, D. B., and J. J. O'Brien, Satellite microwave measurements of surface wind speed in the tropical Pacific, *Trop. Ocean Atmos. Newsl.*, *11*, 2–4, 1982.

Chereskin, T. K., J. N. Moum, P. J. Stabeno, D. R. Caldwell, and C. A. Paulson, Fine-scale variability at 140°W in the equatorial Pacific, *J. Geophys. Res.*, *91*, 12,887–12,897, 1986.

Daley, R., The effect of serially correlated observation and model error on atmospheric data assimilation, *Mon. Weather Rev.*, *120*, 164–177, 1992a.

Daley, R., The lagged innovation covariance: A performance diagnostic for atmospheric data assimilation, *Mon. Weather Rev.*, *120*, 178–196, 1992b.

Dee, D. P., S. E. Cohn, and M. Ghil, An efficient algorithm for estimating noise covariance in distributed systems, *IEEE Trans. Autom. Control*, *AC-30*, 1057–1065, 1985.

Eriksen, C. C., M. B. Blumenthal, S. P. Hayes, and P. Ripa, Wind-generated equatorial Kelvin waves observed across the Pacific Ocean, *J. Phys. Oceanogr.*, *13*, 1622–1640, 1983.

Fu, L-L., I. Fukumori, and R. N. Miller, Fitting dynamic models to the Geosat sea level observations in the tropical Pacific ocean, II, A linear, wind-driven model, *J. Phys. Oceanogr.*, *23*, 2162–2181, 1993.

Gaspar, P., and C. Wunsch, Estimates from altimeter data of barotropic Rossby waves in the northwestern Atlantic ocean, *J. Phys. Oceanogr.*, *19*, 1821–1844, 1989.

Gelb, A. (Ed.), *Applied Optimal Estimation*, 374 pp., MIT Press, Cambridge, Mass., 1974.

Gent, P., and M. A. Cane, A reduced gravity primitive equation model of the upper equatorial ocean, *J. Comput. Phys.*, *81*, 444–480, 1989.

Ghil, M., and P. Malanotte-Rizzoli, Data assimilation in meteorology and oceanography, *Adv. Geophys.*, *33*, 141–266, 1991.

Ghil, M., S. E. Cohn, J. Tavantzis, K. Bube, and E. Isaacson, Applications of estimation theory to numerical weather prediction, in *Dynamic Meteorology: Data Assimilation Methods*, edited by L. Bengtsson, M. Ghil, and E. Kallen, pp. 139–224, Springer-Verlag, New York, 1981.

Halpern, D., and D. E. Harrison, Intercomparison of tropical Pacific mean November 1979 surface wind fields, *Rep. 82-1*, 40 pp., Dep. of Meteorol. and Phys. Oceanogr., Mass. Inst. of Technol., Cambridge, 1982.

Halpern, D., and F. Wentz, On the problem of measuring interannual wind speed variations using SSMI data, *Geophys. Res. Lett.*, *21*, 193–196, 1994.

Hao, Z., and M. Ghil, Data assimilation in a simple tropical ocean model with wind-stress errors, *J. Phys. Oceanogr.*, *24*, 2111–2128, 1994.

Hayes, S. P., L. J. Mangum, J. Picaut, and K. Takeuchi, TOGA-TAO: A moored array for real-time measurements in the tropical Pacific ocean, *Bull. Am. Meteorol. Soc.*, *72*, 339–347, 1991.

Kailath, T., An innovations control approach to least square estimation, I, Linear filtering in additive white noise, *IEEE Trans. Autom. Control*, *13*, 646–655, 1968.

Kawabe, M., Mechanisms of interannual variations of equatorial sea level associated with El Niño, *J. Phys. Oceanogr.*, *24*, 979–993, 1994.

Kessler, W. S., and B. A. Taft, Dynamic height and zonal geostrophic transports in the central tropical Pacific during 1979–1984, *J. Phys. Oceanogr.*, *17*, 97–122, 1987.

Legler, D. M., and J. J. O'Brien, *Atlas of Tropical Pacific Wind-stress Climatology 1971–1980*, 187 pp., Florida State University, Tallahassee, 1985.

Levitus, S., Climatological atlas of the world ocean, *NOAA Prof. Pap. 13*, 173 pp., U.S. Govt. Print. Office, Washington, D.C., 1982.

McPhaden, M. J., A. J. Busalacchi, J. Picaut, and G. Raymond, A model study of potential sampling errors due to data scatter around expendable bathythermograph transects in the tropical Pacific, *J. Geophys. Res.*, *93*, 8119–8130, 1988.

Meyers, G., H. Phillips, N. Smith, and J. Sprintall, Space and time scales for optimal interpolation of temperature – tropical Pacific ocean, *Prog. Oceanogr.*, *28*, 189–218, 1991.

Miller, R. N., Toward the application of the Kalman filter to regional open ocean modeling, *J. Phys. Oceanogr.*, *16*, 773–790, 1986.

Miller, R. N., Tropical data assimilation experiments with simulated data: The impact of the Tropical Ocean and Global Atmosphere Thermal Array for the Ocean, *J. Geophys. Res.*, *95*, 11,461–11,482, 1990.

Miller, R. N., and M. A. Cane, A Kalman filter analysis of sea level height in the tropical Pacific, *J. Phys. Oceanogr.*, *19*, 773–790, 1989.

Moore, A. M., and D. L. T. Anderson, The assimilation of XBT data into a layer model of the tropical Pacific ocean, *Dyn. Atmos. Oceans*, *13*, 441–464, 1989.

Picaut, J., and R. Tournier, Monitoring the 1979–85 equatorial Pacific current transports with expendable bathythermograph data, *J. Geophys. Res.*, *96*, 3263–3277, 1991.

Picaut, J., R. Tournier, and V. Fabre, Atlas des températures et des courants géostrophiques de 1979 a 1985 deduits des mesures XBT le long de rails de navigation du Pacifique tropical, *Sci. and Tech. Rep. 4*, 83 pp., Sci. de la Mer, Oceanogr. Phys., Office de la Rech. Sci. and Tech. d'Outre-Mer, Nouméa, 1991.

Rebert, J. P., J. R. Donguy, G. Eldin, and K. Wyrtki, Relations between sea level, thermocline depth, heat content, and dynamic height in the tropical Pacific ocean, *J. Geophys. Res.*, *90*, 11,719–11,725, 1985.

Reynolds, R. W., K. Arpe, C. Gordon, S. P. Hayes, A. Leetmaa, and M. McPhaden, A comparison of tropical Pacific wind analyses, *J. Clim.*, *2*, 105–111, 1989.

Sadler, J. C., and B. J. Kilonsky, Deriving surface winds from satellite observations of low- level cloud motions, *J. Clim. Appl. Meteorol.*, *24*, 758–769, 1985.

Sadler, J. C., M. A. Lander, A. M. Hori, and L. K. Oda, Tropical marine climate atlas, II, Pacific Ocean, *Tech. Rep. UHMET 87-02*, 27 pp., Dep. of Meteorol., Univ. of Hawaii, Honolulu, 1987.

Shapiro, R., The use of linear filtering as a parameterization of atmospheric diffusion, *J. Atmos. Sci.*, *28*, 523–531, 1971.

Sheinbaum, J., and D. L. T. Anderson, Variational assimilation of XBT data, II, Sensitivity studies and the use of smoothing constraints, *J. Phys. Oceanogr.*, *20*, 689–704, 1990.

Stricherz, J. N., J. J. O'Brien, and D. M. Legler, Atlas of Florida State University Tropical Pacific Winds for TOGA, Mesoscale Air-Sea Interaction Group technical report, 261 pp., Fla. State Univ., Tallahassee, 1992.

Taft, B. A., and W. S. Kessler, Variations of zonal currents in the central tropical Pacific during 1970 to 1987: Sea level and dynamic height measurements, *J. Geophys. Res.*, *96*, 12,599–12,618, 1991.

Wyrtki, K., K. Constantine, B. J. Kilonsky, G. Mitchum, B. Miyamoto, T. Murphy, S. Nakahara, and P. Caldwell, The Pacific Island Sea Level Network, *JIMAR Contrib. 88-0137, Data Rep. 002*, 71 pp., Joint Inst. for Mar. and Atmos. Res., Univ. of Hawaii, Honolulu, 1988.

Zebiak, S. E., Oceanic heat content variability and El Niño cycles, *J. Phys. Oceanogr.*, *19*, 475–486, 1989.

A. J. Busalacchi, Laboratory for Hydrospheric Processes, NASA Goddard Space Flight Center, Greenbelt, MD 20771.

E. C. Hackert, Hughes STX Corporation and Laboratory for Hydrospheric Processes, NASA Goddard Space Flight Center, Greenbelt, MD 20771.

R. N. Miller, College of Oceanic and Atmospheric Sciences, Oregon State University, Oceanography Administration Building 104, Corvallis, OR 97331-5503.